

Highlights

A polyhedral scaled boundary finite element method solving three-dimensional heat conduction problems

Mingjiao Yan, Yang Yang, Chao Su, Zongliang Zhang, Qingsong Duan, Dengmiao Hao, Jian Zhou

- Derived a semi-analytical formulation to solve heat conduction problems based on the SBFEM
- Developed a polyhedral SBFEM (PSBFEM) framework incorporating Wachspress shape functions
- Implemented the PSBFEM in ABAQUS UEL to solve both steady-state and transient heat conduction problems
- Achieved superior accuracy with the PSBFEM compared to the FEM during mesh refinement
- Polyhedral elements provide an efficient solution for complex simulations by significantly reducing computational costs

A polyhedral scaled boundary finite element method solving three-dimensional heat conduction problems

Mingjiao Yan^a, Yang Yang^b, Chao Su^a, Zongliang Zhang^b, Qingsong Duan^c,
Dengmiao Hao^a, Jian Zhou^d

^a*College of Water Conservancy and Hydropower Engineering, Hohai University, Nanjing, 210098, Jiangsu, China*

^b*PowerChina Kunming Engineering Corporation Limited, Kunming, 650051, Yunnan, China*

^c*College of Water Conservancy, Yunnan Agricultural University, Kunming, 650201, Yunnan, China*

^d*Water Conservancy Construction and Quality Safety Management Service Center of Zhenyuan Yi, Hani and Lahu Autonomous County, Pu'er, 666599, Yunnan, China*

Abstract

In this study, we derived a three-dimensional scaled boundary finite element formulation for heat conduction problems. By incorporating Wachspress shape functions, a polyhedral scaled boundary finite element method (PSBFEM) was proposed to address heat conduction challenges in complex geometries. To address the complexity of traditional methods, this work introduced polygonal discretization techniques that simplified the topological structure of the polyhedral mesh and effectively integrated polyhedral and octree meshes, thereby reducing the number of element faces and enhancing mesh efficiency to accommodate intricate shapes. The developed formulation supported both steady-state and transient heat conduction analyses and was implemented in ABAQUS through a user-defined element (UEL). Through a series of numerical examples, the accuracy and convergence of the proposed

method were validated. The results indicated that the PSBFEM consistently achieved higher accuracy than the FEM as the mesh was refined. The polyhedral elements offered a computationally efficient solution for complex simulations, significantly reducing computational costs. [Additionally, by utilizing the octree mesh parent element acceleration technique, the computational efficiency of PSBFEM surpassed that of the FEM.](#)

Keywords: Heat conduction, SBFEM, Polyhedral element, Octree mesh, ABAQUS UEL, Acceleration technology

1. Introduction

Heat conduction problems are prevalent in modern engineering applications, such as electronic device cooling [1], material processing [2], nuclear reactor design [3], and civil engineering [4]. Accurately and efficiently solving three-dimensional (3D) heat conduction problems is essential for optimizing designs and enhancing system performance. Experimentation is often employed to study heat conduction phenomena [5, 6]. However, these methods can be time-consuming and costly, potentially failing to capture all the nuances of the system, particularly in geometrically intricate or dynamically varying scenarios. Additionally, although analytical methods [7, 8] have been used over the past decades, they are typically limited by the complexities of geometry and boundary conditions. Consequently, numerical methods, particularly finite element method (FEM), have become indispensable for addressing complex heat conduction problems [9, 10].

In traditional 3D FEM, tetrahedral and hexahedral elements are widely utilized. However, the accuracy and reliability of FEM solutions depend heavily on mesh quality. Tetrahedral elements allow for automated mesh generation but often result in lower accuracy, while hexahedral elements provide higher accuracy but require manual intervention during the mesh generation process, making it more time-consuming. To achieve precision in computational results, high-quality meshes are typically generated through complex and time-consuming re-meshing algorithms. According to Sandia National Laboratories, preprocessing steps such as mesh generation account for more than 80% of the total analysis time [11]. To alleviate the burden of preprocessing, researchers have explored various alternative methods, including the boundary element method (BEM) [12], isogeometric analysis (IGA) [13], meshfree methods [14], and physics-informed neural networks (PINNs) [15]. Each of these methods aims to address specific challenges posed by the FEM, particularly in terms of geometric complexity and computational cost, yet they present their own limitations in practice.

For large-scale problems, employing a locally refined mesh in regions of interest has become a common strategy, as it provides higher accuracy in critical areas while reducing the overall computational load [16]. This approach has given rise to non-matching mesh techniques, which allow for tailored meshing strategies that apply finer meshes where needed and coarser meshes elsewhere [17, 18]. However, non-matching meshes introduce the challenge of handling hanging nodes—nodes that do not align with those in adjacent

elements. Traditional FEM struggles with such nodes due to the disruption of continuity and compatibility conditions, which are essential for accurate solutions [19].

Several techniques have been developed to manage hanging nodes, including the Arlequin method [20], the mortar segment-to-segment method [21], multi-point constraint equations [22], and the polygonal finite element method (PFEM) [23, 24]. Among these, the PFEM inherently addresses non-matching mesh problems by treating hanging nodes as part of the element discretization. However, the PFEM's reliance on a weak formulation in each discretization direction often results in reduced computational accuracy.

The scaled boundary finite element method (SBFEM) has emerged as a robust technique for handling hanging nodes in quadtree and octree meshes [25, 26]. The SBFEM combines the strengths of both the FEM and the BEM into a semi-analytical approach. Discretization occurs only in the circumferential direction, while the radial direction retains a strong form of the governing equations. This hybrid approach enables significant computational efficiency, making it well-suited for complex engineering applications [27]. The SBFEM's ability to handle irregular meshes and discontinuities while maintaining high precision has led to its widespread application in various fields [28, 29, 30].

Moreover, to enhance the capability of SBFEM in handling complex geometries, researchers have introduced polygonal and polyhedral techniques. Ye et al. [29, 31] integrated standard SBFEM with a polygonal mesh tech-

nique to address static and dynamic problems. Natarajan et al. [32] developed an SBFEM for 3D convex polyhedra by employing surface discretization with Wachspress interpolants, ensuring high accuracy in linear elasticity. Furthermore, to accurately capture the complex geometries of polygonal and quadtree elements, researchers [32, 33, 34] introduced a NURBS-based polygonal SBFEM by incorporating non-uniform rational B-splines (NURBS), enabling precise representation of curved boundaries. These advancements have significantly enhanced the flexibility and accuracy of SBFEM, establishing it as a powerful tool for various engineering applications.

Currently, no dedicated software exists for polyhedral SBFEM. Researchers typically implement this method through secondary development based on commercial software. Ya et al. [35] extended SBFEM to address interfacial problems using polyhedral meshes in ABAQUS UEL. Yang et al. [36] developed UEL and VUEL implementations in ABAQUS to perform static and elasto-dynamic stress analyses of solids. However, these approaches discretize the boundary surfaces using quadrilateral and triangular elements, resulting in polyhedral elements with relatively complex topologies.

Recent studies have extended SBFEM to heat conduction problems. For instance, Bazzyar et al. [37] used the SBFEM to solve 2D heat conduction problems in anisotropic media. Yu et al. [38] applied a hybrid quadtree mesh in SBFEM to analyze transient heat conduction problems involving cracks or inclusions. Yang et al. [39] developed a user element (UEL) of polygonal SBFEM to solve 2D heat conduction problems. However, most current

research focuses on 2D problems. He et al. [40] presented a novel numerical technique that combines the quadtree technique, SBFEM, image-based modeling, and inverse analysis to evaluate the effective thermal conductivity of heterogeneous materials. He et al. [41] proposed a new adaptive algorithm integrating quadtree SBFEM and the smoothed effective heat capacity method for phase-change heat transfer problems. Wang et al. [42] developed a numerical model using SBFEM-based basis functions to bridge small and large scales in heat conduction, ensuring both efficiency and accuracy for complex geometries. For 3D heat conduction problems, Lu et al. [43] developed a modified SBFEM to address steady-state heat conduction problems, but transient analysis remains underexplored.

In this study, a polyhedral SBFEM (PSBFEM) framework is proposed for solving 3D steady-state and transient heat conduction problems. The remainder of this paper is organized as follows: Sections 2 and 3 derive the formulation of the SBFEM for 3D heat conduction analysis. Section 4 develops a PSBFEM by incorporating Wachspress shape functions. Section 5 presents the solution procedure for the SBFEM equations. Section 6 describes the implementation process for solving heat conduction problems using the SBFEM in ABAQUS UEL. Section 7 provides several numerical examples to demonstrate the accuracy and efficiency of the proposed method. Finally, Section 8 concludes the study by summarizing the key findings.

2. Governing equations of the 3D heat conduction problems

In this study, we considered a 3D transient heat conduction problem, the governing equations without heat sources are written as [43, 44]

$$\mathbf{L}^T \mathbf{q} + \rho c \dot{T} = 0 \quad \text{in} \quad \Omega, \quad (1)$$

where ρ denotes the mass density. c is the heat capacity, \dot{T} is the temperature change rate, Ω denotes the computational domain; \mathbf{q} is the heat flux vector, \mathbf{q} can be expressed as

$$\mathbf{q} = -\mathbf{k} \mathbf{L} T, \quad (2)$$

where T is the temperature, \mathbf{k} is the matrix of the thermal conductivity, \mathbf{k} can be written as:

$$\mathbf{k} = \begin{bmatrix} k_x & 0 & 0 \\ 0 & k_y & 0 \\ 0 & 0 & k_z \end{bmatrix}, \quad (3)$$

where k_x , k_y , and k_z are the thermal conductivity in the x, y, and z directions, respectively. The operator \mathbf{L} is the differential operator and can be written as

$$\mathbf{L} = \begin{Bmatrix} \frac{\partial}{\partial x} \\ \frac{\partial}{\partial y} \\ \frac{\partial}{\partial z} \end{Bmatrix}. \quad (4)$$

The initial conditions can be written as follows:

$$T(x, y, z, t = 0) = T_0(x, y, z) \quad \text{in} \quad \Omega. \quad (5)$$

where T_0 denotes the initial temperature. And the boundary conditions can be expressed as:

$$T(x, y, z) = \bar{T} \quad \text{on} \quad S_1, \quad (6)$$

$$-k \frac{\partial T}{\partial n} = \bar{q}_n = \begin{cases} q_2 & \text{on} \quad S_2 \\ h(T - T_\infty) & \text{on} \quad S_3 \end{cases}, \quad (7)$$

where n is outward normal vector to Ω . S is the boundary. In addition, \bar{T} and q_2 denote the specified boundary temperature and heat flux, respectively, while h represents the convection heat transfer coefficient, and T_∞ is the surrounding temperature.

Applying the Fourier transform to Eq. (1) yields the governing equation in the frequency domain as follows:

$$\mathbf{L}^T \tilde{\mathbf{q}} + i\omega\rho c \tilde{T} = 0, \quad (8)$$

where $\tilde{\mathbf{q}}$ and \tilde{T} are the Fourier transform of \mathbf{q} and T , respectively. ω is the frequency. When $\omega = 0$, the problem reduces to a steady-state heat conduction scenario.

3. Formulation of SBFEM for heat conduction problems

3.1. Scaled boundary transformation of the geometry

The scaled boundary coordinates is shown in Fig. 1. The Cartesian coordinates of a point $(\hat{x}, \hat{y}, \hat{z})$ within the volume sector V_e can be defined by the scaled boundary coordinates (ξ, η, ζ) as [45, 27]

$$\hat{x}(\xi, \eta, \zeta) = \xi \hat{x}(\eta, \zeta) = \xi \mathbf{N}(\eta, \zeta) \hat{\mathbf{x}}, \quad (9a)$$

$$\hat{y}(\xi, \eta, \zeta) = \xi \hat{y}(\eta, \zeta) = \xi \mathbf{N}(\eta, \zeta) \hat{\mathbf{y}}, \quad (9b)$$

$$\hat{z}(\xi, \eta, \zeta) = \xi \hat{z}(\eta, \zeta) = \xi \mathbf{N}(\eta, \zeta) \hat{\mathbf{z}}, \quad (9c)$$

where $\hat{\mathbf{x}}$, $\hat{\mathbf{y}}$ and $\hat{\mathbf{z}}$ denote the nodal coordinate vectors of the surface element S_e in Cartesian coordinates. $\mathbf{N}(\eta, \zeta)$ is the shape function vector

$$\mathbf{N}(\eta, \zeta) = [N_1(\eta, \zeta) \quad N_2(\eta, \zeta) \quad \dots \quad N_n(\eta, \zeta)], \quad (10)$$

where $N_n(\eta, \zeta)$ denotes the shape function and n represents the total number of nodes in the polygon.

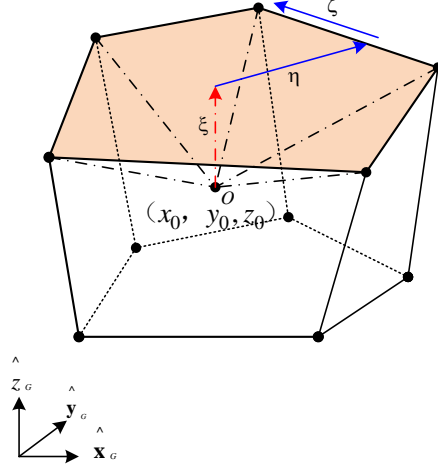


Fig. 1. Scaled boundary coordinates (ξ, η, ζ) representing the coordinate system centered at O for an arbitrary faceted polyhedron.

The partial derivatives with respect to the scaled boundary coordinates are connected to those in Cartesian coordinates by the following equation:

$$\begin{Bmatrix} \frac{\partial}{\partial \xi} \\ \frac{\partial}{\partial \eta} \\ \frac{\partial}{\partial \zeta} \end{Bmatrix} = \begin{bmatrix} 1 & 0 & 0 \\ 0 & \xi & 0 \\ 0 & 0 & \xi \end{bmatrix} \mathbf{J}_{\mathbf{b}}(\eta, \zeta) \begin{Bmatrix} \frac{\partial}{\partial \hat{x}} \\ \frac{\partial}{\partial \hat{y}} \\ \frac{\partial}{\partial \hat{z}} \end{Bmatrix}, \quad (11)$$

where $\mathbf{J}_{\mathbf{b}}(\eta, \zeta)$ is the Jacobian matrix on the boundary ($\xi = 1$), and is defined as follows:

$$\mathbf{J}_{\mathbf{b}}(\eta, \zeta) = \begin{bmatrix} \hat{x}(\eta, \zeta) & \hat{y}(\eta, \zeta) & \hat{z}(\eta, \zeta) \\ \hat{x}(\eta, \zeta)_{,\eta} & \hat{y}(\eta, \zeta)_{,\eta} & \hat{z}(\eta, \zeta)_{,\eta} \\ \hat{x}(\eta, \zeta)_{,\zeta} & \hat{y}(\eta, \zeta)_{,\zeta} & \hat{z}(\eta, \zeta)_{,\zeta} \end{bmatrix}. \quad (12)$$

The determinant of $\mathbf{J}_{\mathbf{b}}(\eta, \zeta)$ is given by the following expression:

$$|\mathbf{J}_{\mathbf{b}}| = \hat{x}(\hat{y}_{,\eta}\hat{z}_{,\zeta} - \hat{z}_{,\eta}\hat{y}_{,\zeta}) + \hat{y}(\hat{z}_{,\eta}\hat{x}_{,\zeta} - \hat{x}_{,\eta}\hat{z}_{,\zeta}) + \hat{z}(\hat{x}_{,\eta}\hat{y}_{,\zeta} - \hat{y}_{,\eta}\hat{x}_{,\zeta}), \quad (13)$$

where the argument (η, ζ) are omitted for simplicity. From Eq. (11), it follows that the inverse relationship is expressed as:

$$\begin{Bmatrix} \frac{\partial}{\partial \hat{x}} \\ \frac{\partial}{\partial \hat{y}} \\ \frac{\partial}{\partial \hat{z}} \end{Bmatrix} = \mathbf{J}_{\mathbf{b}}^{-1}(\eta, \zeta) \begin{Bmatrix} \frac{\partial}{\partial \xi} \\ \frac{1}{\xi} \frac{\partial}{\partial \eta} \\ \frac{1}{\xi} \frac{\partial}{\partial \zeta} \end{Bmatrix}, \quad (14)$$

where the inverse of the Jacobian matrix at the boundary, $\mathbf{J}_{\mathbf{b}}^{-1}(\eta, \zeta)$, can be expressed as follows:

$$\mathbf{J}_{\mathbf{b}}^{-1}(\eta, \zeta) = \frac{1}{|\mathbf{J}_{\mathbf{b}}|} \begin{bmatrix} y_{,\eta}z_{,\zeta} - z_{,\eta}y_{,\zeta} & zy_{,\zeta} - yz_{,\zeta} & yz_{,\eta} - zy_{,\eta} \\ z_{,\eta}x_{,\zeta} - x_{,\eta}z_{,\zeta} & xz_{,\zeta} - zx_{,\zeta} & zx_{,\eta} - xz_{,\eta} \\ x_{,\eta}y_{,\zeta} - y_{,\eta}x_{,\zeta} & yx_{,\zeta} - xy_{,\zeta} & xy_{,\eta} - yx_{,\eta} \end{bmatrix}. \quad (15)$$

Hence, Eq. (14) can also be expressed as

$$\begin{aligned}
\left\{ \begin{array}{l} \frac{\partial}{\partial \bar{x}} \\ \frac{\partial}{\partial \bar{y}} \\ \frac{\partial}{\partial \bar{z}} \end{array} \right\} &= \frac{1}{|\mathbf{J}_{\mathbf{b}}|} \begin{bmatrix} y_{,\eta} z_{,\zeta} - z_{,\eta} y_{,\zeta} \\ z_{,\eta} x_{,\zeta} - x_{,\eta} z_{,\zeta} \\ x_{,\eta} y_{,\zeta} - y_{,\eta} x_{,\zeta} \end{bmatrix} \frac{\partial}{\partial \xi} \\
&+ \frac{1}{\xi} \left(\frac{1}{|\mathbf{J}_{\mathbf{b}}|} \begin{bmatrix} zy_{,\zeta} - yz_{,\zeta} \\ xz_{,\zeta} - zx_{,\zeta} \\ yx_{,\zeta} - xy_{,\zeta} \end{bmatrix} \frac{\partial}{\partial \eta} + \frac{1}{|\mathbf{J}_{\mathbf{b}}|} \begin{bmatrix} yz_{,\eta} - zy_{,\eta} \\ zx_{,\eta} - xz_{,\eta} \\ xy_{,\eta} - yx_{,\eta} \end{bmatrix} \frac{\partial}{\partial \zeta} \right). \tag{16}
\end{aligned}$$

The gradient operator in the Cartesian coordinate system can be converted to the scaled boundary coordinate system as follows:

$$\mathbf{L} = \mathbf{b}_1(\eta, \zeta) \frac{\partial}{\partial \xi} + \frac{1}{\xi} \left(\mathbf{b}_2(\eta, \zeta) \frac{\partial}{\partial \eta} + \mathbf{b}_3(\eta, \zeta) \frac{\partial}{\partial \zeta} \right), \tag{17}$$

where $\mathbf{b}_1(\eta, \zeta)$, $\mathbf{b}_2(\eta, \zeta)$, and $\mathbf{b}_3(\eta, \zeta)$ can be defined as

$$\mathbf{b}_1(\eta, \zeta) = \frac{1}{|\mathbf{J}_b|} \begin{bmatrix} y_{,\eta}z_{,\zeta} - z_{,\eta}y_{,\zeta} \\ z_{,\eta}x_{,\zeta} - x_{,\eta}z_{,\zeta} \\ x_{,\eta}y_{,\zeta} - y_{,\eta}x_{,\zeta} \end{bmatrix}, \quad (18)$$

$$\mathbf{b}_2(\eta, \zeta) = \frac{1}{|\mathbf{J}_b|} \begin{bmatrix} zy_{,\zeta} - yz_{,\zeta} \\ xz_{,\zeta} - zx_{,\zeta} \\ yx_{,\zeta} - xy_{,\zeta} \end{bmatrix}, \quad (19)$$

$$\mathbf{b}_3(\eta, \zeta) = \frac{1}{|\mathbf{J}_b|} \begin{bmatrix} yz_{,\eta} - zy_{,\eta} \\ zx_{,\eta} - xz_{,\eta} \\ xy_{,\eta} - yx_{,\eta} \end{bmatrix}. \quad (20)$$

3.2. Temperature field

The temperature of any point $\tilde{T}(\xi, \eta, \zeta)$ in the SBFEM coordinates can be written as:

$$\tilde{T}(\xi, \eta, \zeta) = \mathbf{N}(\eta, \zeta)\tilde{T}(\xi), \quad (21)$$

where $\tilde{T}(\xi)$ is the nodal temperature vector and $\mathbf{N}(\eta, \zeta)$ is the matrix of shape function.

By using Eqs. (21) and (17), yields the temperature field partial derivatives as follows:

$$\left[\frac{\partial \tilde{T}}{\partial \hat{x}} \quad \frac{\partial \tilde{T}}{\partial \hat{y}} \quad \frac{\partial \tilde{T}}{\partial \hat{z}} \right]^T = \mathbf{b}_1(\eta, \zeta) \frac{\partial \tilde{T}}{\partial \xi} + \frac{1}{\xi} \left(\mathbf{b}_2(\eta, \zeta) \frac{\partial \tilde{T}}{\partial \eta} + \mathbf{b}_3(\eta, \zeta) \frac{\partial \tilde{T}}{\partial \zeta} \right). \quad (22)$$

For simplicity, Eq. (22) can be rewritten by substituting the temperature expression from Eq. (21), as follows:

$$\left[\frac{\partial \tilde{T}}{\partial \hat{x}} \quad \frac{\partial \tilde{T}}{\partial \hat{y}} \quad \frac{\partial \tilde{T}}{\partial \hat{z}} \right]^T = \mathbf{B}_1(\eta, \zeta) \tilde{T}_{,\xi} + \frac{1}{\xi} \mathbf{B}_2(\eta, \zeta) \tilde{T}, \quad (23)$$

where

$$\mathbf{B}_1(\eta, \zeta) = \mathbf{b}_1(\eta, \zeta) \mathbf{N}(\eta, \zeta), \quad (24)$$

$$\mathbf{B}_2(\eta, \zeta) = \mathbf{b}_2(\eta, \zeta) \mathbf{N}(\eta, \zeta)_{,\eta} + \mathbf{b}_3(\eta, \zeta) \mathbf{N}(\eta, \zeta)_{,\zeta}. \quad (25)$$

The heat flux $\tilde{\mathbf{q}}(\xi, \eta, \zeta)$ can be represented in the coordinate system of the SBFEM as follows:

$$\tilde{\mathbf{q}}(\xi, \eta, \zeta) = -\mathbf{k} \left(\mathbf{B}_1(\eta, \zeta) \tilde{T}(\xi)_{,\xi} + \frac{1}{\xi} \mathbf{B}_2(\eta, \zeta) \tilde{T}(\xi) \right). \quad (26)$$

3.3. Scaled boundary finite element equation

By employing the method of weighted residuals [44], Eq. (8) can be transformed into

$$\begin{aligned} & \int_{\Omega} w \mathbf{b}_1^T \tilde{\mathbf{q}}_{,\xi} \, d\Omega + \int_{\Omega} w \frac{1}{\xi} (\mathbf{b}_2^T \tilde{\mathbf{q}}_{,\eta} + \mathbf{b}_3^T \tilde{\mathbf{q}}_{,\zeta}) \, d\Omega \\ & + i\omega \int_{\Omega} w \rho c \tilde{T} \, d\Omega = 0. \end{aligned} \quad (27)$$

where $w = w(\xi, \eta, \zeta)$ is the weighting function. Following the procedures outlined by [44], we further simplify Eq. (27) as follows (see Appendix A for the detailed derivation):

$$\begin{aligned} & \mathbf{E}_0 \xi^2 \tilde{T}(\xi)_{,\xi\xi} + (2\mathbf{E}_0 - \mathbf{E}_1 + \mathbf{E}_1^T) \xi \tilde{T}(\xi)_{,\xi} \\ & + (\mathbf{E}_1^T - \mathbf{E}_2) \tilde{T}(\xi) - \mathbf{M}_0 i\omega \xi^2 \tilde{T}(\xi) = \xi \mathbf{F}(\xi), \end{aligned} \quad (28)$$

where the global coefficient matrices \mathbf{E}_0 , \mathbf{E}_1 , \mathbf{E}_2 and \mathbf{M}_0 for the entire element are formed by assembling the local coefficient matrices \mathbf{E}_0^e , \mathbf{E}_1^e , \mathbf{E}_2^e and \mathbf{M}_0^e corresponding to each surface element. These local matrices for a surface element S_e can be expressed as follows:

$$\mathbf{E}_0^e = \int_{S_e} \mathbf{B}_1^T \mathbf{k} \mathbf{B}_1 |\mathbf{J}_b| \, d\eta d\zeta, \quad (29)$$

$$\mathbf{E}_1^e = \int_{S_e} \mathbf{B}_2^T \mathbf{k} \mathbf{B}_1 |\mathbf{J}_b| \, d\eta d\zeta, \quad (30)$$

$$\mathbf{E}_2^e = \int_{S_e} \mathbf{B}_2^T \mathbf{k} \mathbf{B}_2 |\mathbf{J}_b| \, d\eta d\zeta, \quad (31)$$

$$\mathbf{M}_0^e = \int_{S_e} \mathbf{N}^T \rho c \mathbf{N} |\mathbf{J}_b| d\eta d\zeta. \quad (32)$$

4. Polyhedral SBFEM element

4.1. Polyhedral element construction

In traditional 3D SBFEM, boundary surfaces are discretized using triangular and quadrilateral elements [35, 36]. As a result, the polyhedra processed by traditional 3D SBFEM exhibit relatively complex topologies, as illustrated in Figs. 2 (a) and (c). The intricate topological geometry of these polyhedra is evident. To address this complexity, this work introduces polygonal discretization techniques that simplify the topological structure of the polyhedra, thereby reducing the number of element faces, as shown in Figs. 2 (b) and (d). From the figures, it is clear that the polyhedra constructed using polygonal discretization significantly reduce the number of element faces, particularly for the octree mesh. This reduction not only enhances mesh efficiency but also provides clearer visualization. Furthermore, Fig. 3 compares the traditional octree mesh with the polygon-based octree mesh surface, highlighting that the polygon-based octree mesh surface is more concise and has fewer faces.

To construct polyhedral elements, we have introduced polygonal techniques. As shown in Fig. 4, the polygonal surface of the polyhedron is first mapped onto a regular polygon. This regular polygon is then subdivided into smaller triangles, and each of these sub-triangles is subsequently mapped onto a standard triangle. Quadrature rules, commonly used in the

FEM for numerical integration, are applied to these sub-triangles to perform the integration.

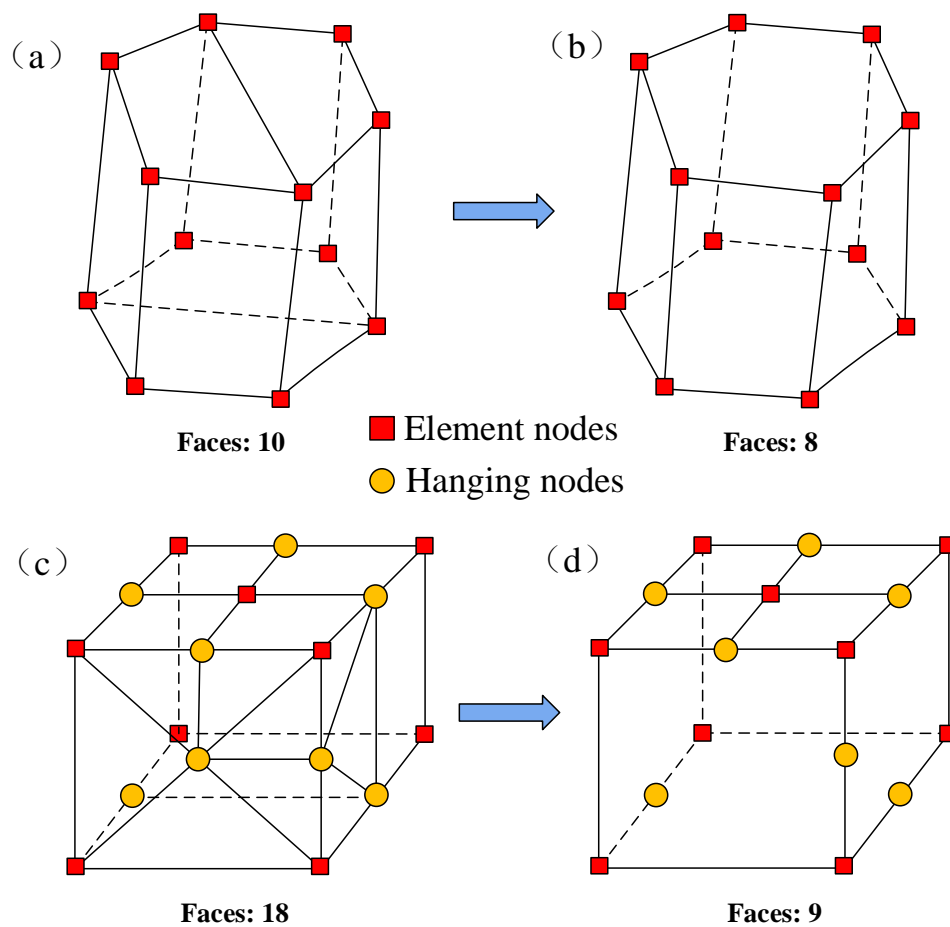


Fig. 2. Polyhedral elements construction based on polygonal surfaces: (a) traditional polyhedral element; (b) polyhedral element constructed from polygonal surfaces; (c) traditional octree element; (d) octree element constructed from polygonal surfaces.

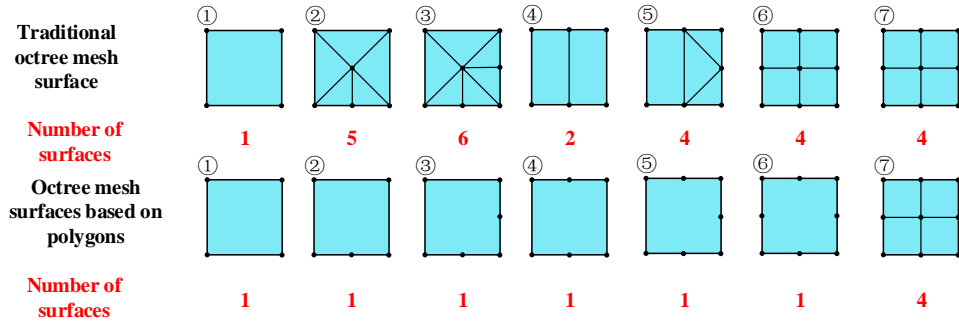


Fig. 3. Comparison of the surfaces between traditional octree mesh and polygon-based octree mesh.

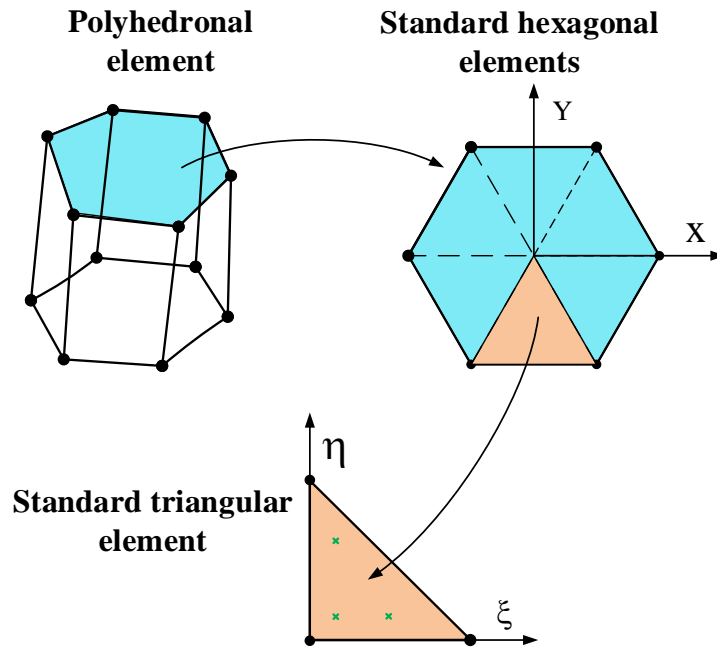


Fig. 4. Numerical integration techniques for arbitrary polytopes.

4.2. Barycentric coordinates over polygonal surfaces

Various methods have been developed for constructing shape functions in polyhedral elements [46], and their comparisons can be found in [47, 48]. The Wachspress shape function, which is based on a rational wedge function and derived using perspective geometry theory for collocation on convex polygon boundaries, is particularly notable for its applicability to arbitrary convex polygons [49]. The Wachspress shape function has several desirable properties, such as the partition of unity, Kronecker-delta function, non-negative, linear precision, etc [50]. Moreover, the key advantage of the Wachspress shape function is its C^∞ smoothness within the polygonal domain and C^0 continuity along the boundaries [51]. Hence, this property enhances the accuracy and ensures the convergence of temperature solutions.

In this work, we focus on using Wachspress shape function to construct conforming approximations on polygonal meshing structures. Wachspress introduced rational basis functions for polygonal elements based on principles from projective geometry. These functions ensure accurate nodal interpolation and maintain linearity along the boundaries by leveraging the algebraic equations of the edges. The polygonal element in Barycentric coordinates is presented in Fig. 5. Let

$$w_k(\mathbf{x}) = \frac{\det(\mathbf{n}_{f_1}, \mathbf{n}_{f_2})}{h_{f_1}(\mathbf{x})h_{f_2}(\mathbf{x})}, \quad (33)$$

where \mathbf{n}_{f_1} and \mathbf{n}_{f_2} denote the normal vectors of the boundary edges. $h_{f_1}(\mathbf{x})$

and $h_{f_2}(\mathbf{x})$ denote the perpendicular distances from \mathbf{x}_k to the facets f_1 and f_2 , which are calculated as follows:

$$h_{f_i}(\mathbf{x}) = (\mathbf{x}_k - \mathbf{x}) \cdot \mathbf{n}_{f_i}. \quad (34)$$

The edges f_i should be arranged in a counterclockwise order around the node \mathbf{x}_k , as viewed from the exterior. The shape functions are then given by [52, 53]

$$\phi_{\mathbf{k}}(\mathbf{x}) = \frac{w_{\mathbf{k}}(\mathbf{x})}{\sum_{\mathbf{k} \in V} w_{\mathbf{k}}(\mathbf{x})}. \quad (35)$$

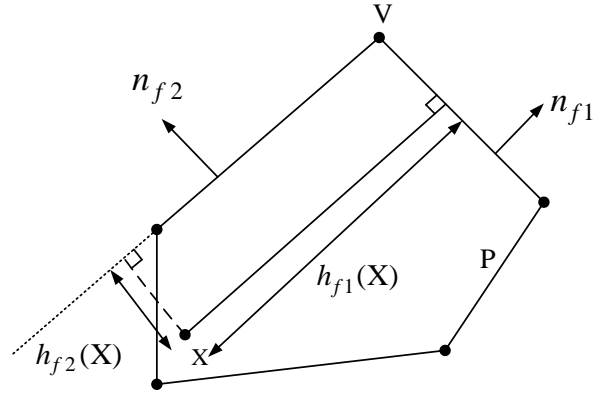


Fig. 5. Barycentric coordinates: Wachspress basis function.

5. Solution procedure

5.1. Stiffness matrix solution

In this study, the $\mathbf{F}(\xi)$ on the right side of Eq. (28) represents the influence of the normal flow rate across the side face. When the domain is enclosed or the side is insulated, $\mathbf{F}(\xi)$ becomes zero [38, 54]. Since we assume an adiabatic side or a closed domain in our analysis, we set $\mathbf{F}(\xi) = \mathbf{0}$. The steady-state temperature field within the SBFEM formulation can be obtained by substituting $\omega = 0$ into Eq. (28), yielding the following result:

$$\mathbf{E}_0 \xi^2 \tilde{T}(\xi)_{,\xi\xi} + (2\mathbf{E}_0 - \mathbf{E}_1 + \mathbf{E}_1^T) \xi \tilde{T}(\xi)_{,\xi} + (\mathbf{E}_1^T - \mathbf{E}_2) \tilde{T}(\xi) = \mathbf{0}. \quad (36)$$

By introducing the variable,

$$\mathbf{X}(\xi) = \begin{bmatrix} \xi^{0.5} \tilde{\mathbf{h}}(\xi) \\ \xi^{-0.5} \tilde{\mathbf{q}}(\xi) \end{bmatrix}, \quad (37)$$

the SBFEM equation can be reformulated as a first-order ordinary differential equation (ODE):

$$\xi \mathbf{X}(\xi)_{,\xi} = \mathbf{Z}_p \mathbf{X}(\xi), \quad (38)$$

where the coefficient matrix \mathbf{Z}_p is a Hamiltonian matrix. \mathbf{Z}_p is expressed as

$$\mathbf{Z}_p = \begin{bmatrix} -\mathbf{E}_0^{-1} \mathbf{E}_1^T + 0.5\mathbf{I} & \mathbf{E}_0^{-1} \\ \mathbf{E}_2 - \mathbf{E}_1 \mathbf{E}_0^{-1} \mathbf{E}_1^T & \mathbf{E}_1 \mathbf{E}_0^{-1} - 0.5\mathbf{I} \end{bmatrix}. \quad (39)$$

The eigenvalue decomposition of \mathbf{Z}_p can be written as

$$\mathbf{Z}_p \begin{bmatrix} \Phi_{h1} & \Phi_{h2} \\ \Phi_{q1} & \Phi_{q2} \end{bmatrix} = \begin{bmatrix} \Phi_{h1} & \Phi_{h2} \\ \Phi_{q1} & \Phi_{q2} \end{bmatrix} \begin{bmatrix} \Lambda^+ & 0 \\ 0 & \Lambda^- \end{bmatrix}, \quad (40)$$

where Φ_{h1} and Φ_{q1} are the corresponding eigenvectors of Λ^+ , and Φ_{h2} and Φ_{q2} are the corresponding eigenvectors of Λ^- . Λ^+ and Λ^- denote the diagonal matrices of eigenvalues with positive and negative real parts, respectively. As a whole, Φ_h and Φ_q is the modal temperature and flux, respectively. [The solution of \$\mathbf{X}\(\xi\)\$ can be written as](#)

$$\mathbf{X}(\xi) = \begin{bmatrix} \Phi_{h1} & \Phi_{h2} \\ \Phi_{q1} & \Phi_{q2} \end{bmatrix} \begin{bmatrix} \xi^{\Lambda^+} & \mathbf{0} \\ \mathbf{0} & \xi^{\Lambda^-} \end{bmatrix} \begin{Bmatrix} \mathbf{c}^n \\ \mathbf{c}^p \end{Bmatrix}, \quad (41)$$

where \mathbf{c}^n and \mathbf{c}^p are the integration constants related to Λ^+ and Λ^- , respectively, and are determined from the boundary conditions. The solution for $\tilde{\mathbf{h}}(\xi)$ and $\tilde{\mathbf{q}}(\xi)$ can be expressed as

$$\tilde{\mathbf{h}}(\xi) = \Phi_{h1} \xi^{-\Lambda^+ - 0.5\mathbf{I}} \mathbf{c}^n, \quad (42)$$

$$\tilde{\mathbf{q}}(\xi) = \Phi_{q1} \xi^{-\Lambda^+ + 0.5\mathbf{I}} \mathbf{c}^n. \quad (43)$$

The relationship between the nodal temperature functions and the nodal flux functions is derived by eliminating the integration constants, as shown

below:

$$\tilde{\mathbf{q}}(\xi) = \mathbf{\Phi}_{q1} \mathbf{\Phi}_{h1}^{-1} \xi \tilde{\mathbf{h}}(\xi). \quad (44)$$

On the boundary ($\xi = 1$), the nodal flux vector is defined as $\mathbf{Q} = \tilde{\mathbf{q}}(\xi = 1)$, and the nodal temperature vector is given by $\mathbf{T} = \tilde{\mathbf{h}}(\xi = 1)$. The relationship between the heat flux and temperature vectors is expressed as $\mathbf{Q} = \mathbf{KT}$. Consequently, the stiffness matrix of the subdomain can be formulated as:

$$\mathbf{K} = \mathbf{\Phi}_{q1} \mathbf{\Phi}_{h1}^{-1}. \quad (45)$$

5.2. Mass matrix solution

The mass matrix for a volume element is expressed as [26, 27]

$$\mathbf{M} = \mathbf{\Phi}_{h1}^{-T} \int_0^1 \xi^{\Lambda^+} \mathbf{m}_0 \xi^{\Lambda^+} \xi d\xi \mathbf{\Phi}_{h1}^{-1}, \quad (46)$$

where the coefficient matrix \mathbf{m}_0 is defined as

$$\mathbf{m}_0 = \mathbf{\Phi}_{h1}^T \mathbf{M}_0 \mathbf{\Phi}_{h1}. \quad (47)$$

By converting the integration component in Eq. (46) into matrix form, the expression for the mass matrix can be rewritten as follows:

$$\mathbf{M} = \mathbf{\Phi}_{h1}^{-T} \mathbf{m} \mathbf{\Phi}_{h1}^{-1}, \quad (48)$$

where

$$\mathbf{m} = \int_0^1 \xi^{\Lambda^+} \mathbf{m}_0 \xi^{\Lambda^+} \xi d\xi. \quad (49)$$

Each element of the matrix \mathbf{m} can be computed analytically, resulting in the following expression:

$$m_{ij} = \frac{m_{0ij}}{\lambda_{ii}^+ + \lambda_{jj}^+ + 2}, \quad (50)$$

where m_{0ij} denotes an entry of \mathbf{m}_0 , and λ_{ij}^+ and λ_{ii}^+ represent specific entries of the matrix Λ^+ .

5.3. Transient solution

The nodal temperature relationship for a bounded domain can be formulated as a standard time-domain equation, utilizing the steady-state stiffness and mass matrices, as follows:

$$\mathbf{KT}(t) + \mathbf{M}\dot{\mathbf{T}}(t) = \mathbf{Q}(t), \quad (51)$$

where the nodal temperature $\mathbf{T}(t)$ is the time-derivative continuous function. Solving for the functional solution in the time domain presents significant challenges. In this study, the backward difference method [55] is employed to solve Eq. (51). The time domain is discretized into discrete time steps, and the solution at each time node is incrementally computed based on the initial conditions. Subsequently, the nodal temperature at any given time is determined through interpolation.

At time $[t, t + \Delta t]$, the temperature change rate $\dot{\mathbf{T}}(t)$ can be expressed as

$$\dot{\mathbf{T}}(t) = \frac{\Delta \mathbf{T}}{\Delta t} = \frac{\mathbf{T}(t)^{t+\Delta t} - \mathbf{T}(t)^t}{\Delta t}. \quad (52)$$

Eq. (52) is substituted into Eq. (51), and the equation at time step $t + \Delta t$ can be obtained as follows:

$$\mathbf{K}^{t+\Delta t} + \frac{\mathbf{M}^{t+\Delta t}}{\Delta t} \mathbf{T}(t)^{t+\Delta t} = \mathbf{Q}(t)^{t+\Delta t} + \frac{\mathbf{M}^{t+\Delta t}}{\Delta t} \mathbf{T}(t)^t. \quad (53)$$

6. Implementation

6.1. Overview framework

This study presents a framework for 3D heat conduction analysis using the PSBFEM with polyhedral and octree meshes, as illustrated in Fig. 6. The framework comprises three submodules: pre-processing, heat conduction analysis, and post-processing. In the pre-processing stage, commercial software such as ANSYS Fluent [56] and STAR-CCM+ [57] is first used to generate polyhedral and octree meshes. A Python script is then employed to convert the mesh data into an ABAQUS input file (.inp). The 3D heat conduction analysis is conducted using an ABAQUS UEL subroutine implemented in FORTRAN. Further implementation details are provided in Section 6.2. Since ABAQUS CAE does not support the visualization of UEL elements, the results are extracted from the output database (.odb) file and visualized using ParaView [58].

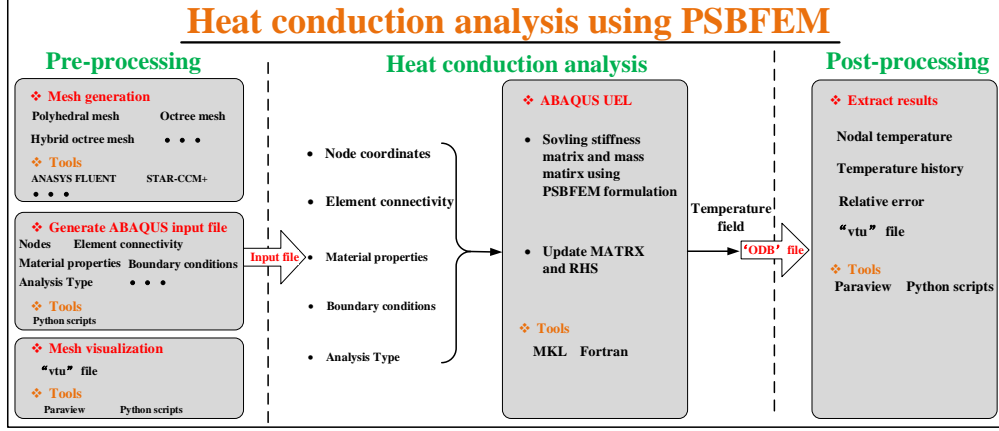


Fig. 6. The framework of PSBFEM solving 3D heat conduction.

6.2. Implementation of the UEL

Algorithm 1 provides a flowchart outlining the procedure for steady-state and transient heat conduction analysis, which has been successfully implemented in ABAQUS using the User Element (UEL) programming interface. The primary function of the UEL in ABAQUS is to update the element’s contribution to the residual force vector (RHS) and the stiffness matrix (AMATRX) via the user subroutine interface provided by the software. For steady-state heat conduction analysis, the AMATRX and the RHS are defined as follows:

$$AMATRX = \mathbf{K}, \tag{54}$$

$$RHS = -\mathbf{K}\mathbf{U}, \tag{55}$$

where \mathbf{U} is the nodal temperature vector.

For the transient heat conduction, AMATRX and RHS are defined as

follows:

$$\mathbf{AMATRIX} = \mathbf{K}^{t+\Delta t} + \frac{\mathbf{M}^{t+\Delta t}}{\Delta t}, \quad (56)$$

$$\text{RHS} = -\mathbf{K}^{t+\Delta t} \mathbf{U}^{t+\Delta t} - \frac{\mathbf{M}^{t+\Delta t}}{\Delta t} (\mathbf{U}^{t+\Delta t} - \mathbf{U}^t). \quad (57)$$

Moreover, it is necessary to construct the element geometry using nodal coordinates and node connectivity information. The element is first constructed to define the numbering and connectivity of the element nodes. As illustrated in Figs. 7 (a) and (b), a hexahedral element and an octahedral element are considered. The numbering of the element faces is defined, followed by the connectivity information of the nodes on each face.

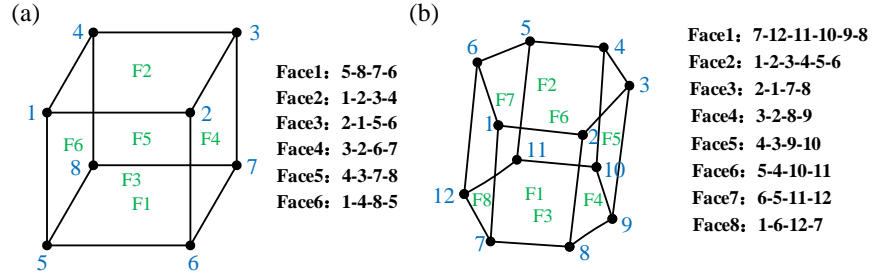


Fig. 7. An example of face numbering for polyhedral elements: (a) hexahedral element; (b) polyhedral element.

6.3. Acceleration technology based on the octree parent element

In large-scale numerical simulations, models are generally made up of numerous elements, each requiring individual computation. Improving the computational efficiency of a single element can therefore lead to faster overall model computation. A key benefit of employing octree discretization is

Algorithm 1 Solving the 3D heat conduction problems using the PSBFEM

Input: Node and element information, material properties, and nodal temperature \mathbf{u}_t

Output: Nodal temperature \mathbf{u}_{t+1}

```
1: while ABAQUS not converged do
2:   Solve nodal temperature  $\mathbf{u}_{t+1}^k$ 
3:   for 1 to AllEle do      ! Traverse all elements
4:     Construct the geometry of elements
5:     Solve the the centre of elements
6:     Solve the coefficient matrices  $\mathbf{E}_0^e, \mathbf{E}_1^e, \mathbf{E}_2^e,$  and  $\mathbf{M}_0^e$  using Eq. (29) ~
Eq. (32)
7:     Construct  $\mathbf{Z}_p$  using Eq. (39)
8:     Solve the  $\mathbf{Z}_p$  by eigenvalue decomposition using Eq. (40)
9:     solve the stiffness  $\mathbf{K}$  and mass matrix  $\mathbf{M}$  using Eq. (45) and Eq.
(48)
10:    if lflags(1)=31 then
11:      Update stiffness matrix AMATRIX and residual force vector
RHS using Eqs. (54) and (55)
12:    end if
13:    if lflags(1)=32 or lflags(1)=33 then
14:      Update stiffness matrix AMATRIX and residual force vector
RHS using Eqs. (56) and (57)
15:    end if
16:  end for
17:  update  $k = k + 1$ 
18:  Solve nodal temperature  $\mathbf{u}_{t+1} = \mathbf{u}_{t+1}^k$ 
19: end while
```

that cubic elements, especially those without hanging nodes, constitute a significant portion of the mesh elements [30, 59].

We define a cubic parent element (without hanging nodes) whose geometric and material parameters are set to 1, as shown in Fig. 8. The mapping relationship between the parent element and the sub-element can be expressed as

$$\mathbf{K}_{sub} = kL\mathbf{K}_{par}, \quad (58)$$

$$\mathbf{M}_{sub} = \rho cL^3\mathbf{M}_{par}, \quad (59)$$

where \mathbf{K}_{sub} and \mathbf{M}_{sub} are the stiffness matrix and mass matrix of the sub-element, respectively, and \mathbf{K}_{par} and \mathbf{M}_{par} are the stiffness matrix and mass matrix of the parent element, respectively. k , ρ , c , and L represent the thermal conductivity, density, heat capacity, and length of the sub-element, respectively.

Before the analysis, the stiffness matrix \mathbf{K}_{par} and mass matrix \mathbf{M}_{par} of the parent element are computed and stored in the computer memory. During the analysis, when the element is a cubic element, the stiffness and mass matrices of the sub-elements are computed based on the mapping relationships in Eqs. (58) and (59). Only the material and geometric coefficients need to be multiplied, eliminating the need to apply the SBFEM method to compute the stiffness and mass matrices. As a result, this approach significantly reduces the computational cost.

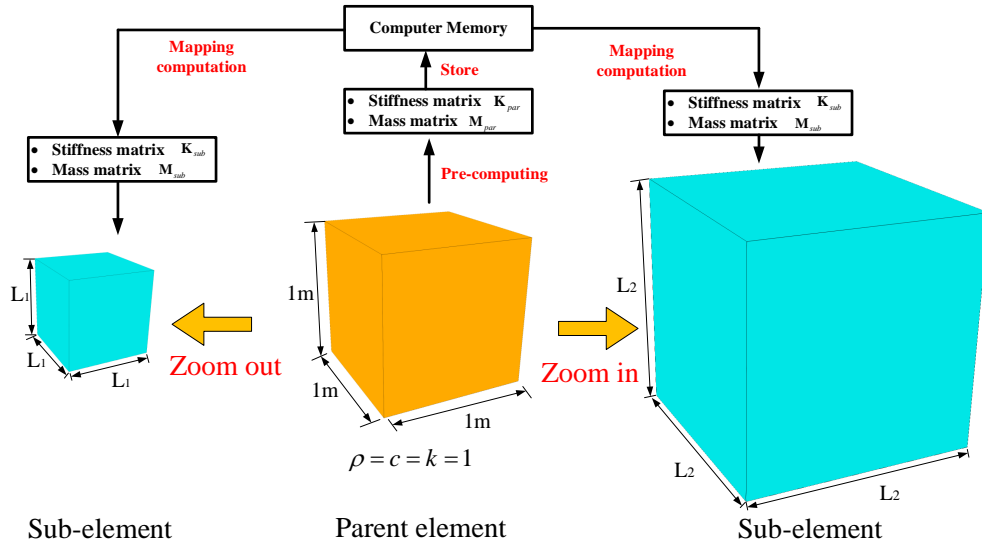


Fig. 8. Mapping relationship between the parent element and sub-element.

6.4. Defining the element of the UEL

In 3D PSBFEM analysis, the geometry of the elements is constructed based on the nodes. Fig. 7 illustrates an example of element construction. Prior to the analysis, it is essential to establish the geometric relationships of the element surfaces according to their numbering, ensuring that the Jacobian matrix remains negative. This requires that the direction of each surface points outward from the element. Fig. 9 shows the supported element types in the PSBFEM. In the PSBFEM, traditional elements such as tetrahedral, wedge, and hexahedral elements can be used. Additionally, the PSBFEM also supports more complex element types, including polyhedral and octree elements. Thus, the PSBFEM serves as an effective tool for solving complex

geometries in numerical analysis

The ABAQUS input file typically provides a comprehensive representation of the numerical model, detailing aspects such as nodes, elements, degrees of freedom, and materials. As shown in Listing 1, the hexahedral element (U8) is defined as follows: Lines 1 to 4 are used to define the pentagonal element (U8). Line 1 specifies the element type, number of nodes, number of element properties, and number of degrees of freedom for each node; Line 2 defines the active degrees of freedom for temperature; Lines 3 and 4 assign the element set labeled **Hexahedron**. Similarly, other elements can be defined using the same procedure.

Listing 1: Input file of the polyhedral element in UEL.

```
1 *USER ELEMENT ,NODES=8 ,TYPE=U8 ,PROPERTIES=5 ,COORDINATES=3 ,  
    VARIABLES=8  
2 11  
3 *Element ,TYPE=U8 ,ELSET=Hexahedron  
4 1, 5, 6, 8, 7, 1, 2, 4, 3  
5 *USER ELEMENT ,NODES=12 ,TYPE=U12 ,PROPERTIES=5 ,COORDINATES=3 ,  
    VARIABLES=12  
6 11  
7 *Element ,TYPE=U12 ,ELSET=Octahedron  
8 2, 7, 8, 9, 10, 11, 12, 1, 2, 3, 4, 5, 6
```

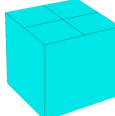
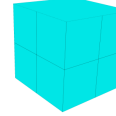
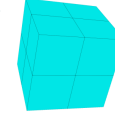
Element type in the PSBFEM				FEM	SBFEM	PSBFEM
Traditional elements						
			...	✓	✓	✓
Polyhedron elements						
			...	✗	✗	✓
Octree elements						
			...	✗	✗	✓

Fig. 9. The supported elements of the PSBFEM.

7. Numerical examples

In this section, several benchmark problems were presented to demonstrate the convergence and accuracy of the proposed framework for heat conduction analysis. Moreover, the results obtained from the PSBFEM were compared with those from the FEM, with the FEM analysis performed using the commercial software ABAQUS. The comparisons were conducted on a system equipped with an Intel Core i5-10210U CPU (1.60 GHz) and 8.0 GB of RAM. To validate the proposed approach, the relative errors e_{L_2} in

temperature were examined as follows:

$$\mathbf{e}_{L_2} = \frac{\|\mathbf{T}_{num} - \mathbf{T}_{ref}\|_{L_2}}{\|\mathbf{T}_{ref}\|_{L_2}}, \quad (60)$$

where \mathbf{T}_{num} is the numerical results and \mathbf{T}_{ref} is the reference solutions.

7.1. Patch test

To verify that the proposed method satisfies the convergence requirement, it must pass the standard patch test [35, 60]. As shown in Fig. 10 (a), the patch test was conducted using a quadrangular prism ($a = 1$ m, $b = 1$ m, $h = 1$ m). The material constants were a thermal conductivity of 1.0 W/m/°C and a volumetric heat capacity of $\rho c = 1.0\text{J}/(\text{m}^3 \cdot ^\circ\text{C})$. Temperatures of $T = 100^\circ\text{C}$ and $T = 0^\circ\text{C}$ were prescribed on the top surface ($z = 3$ m) and bottom surface ($z = 0$ m), respectively. The temperature distribution was shown in Fig. 10 (b). Tab. 1 presented the relative errors for nodal temperatures calculated at all nodes and compared to the analytical solution. The maximum relative error of the proposed method in temperature compared to the analytical solution was 1.53×10^{-4} . Thus, the proposed method passed the patch test with sufficient accuracy.

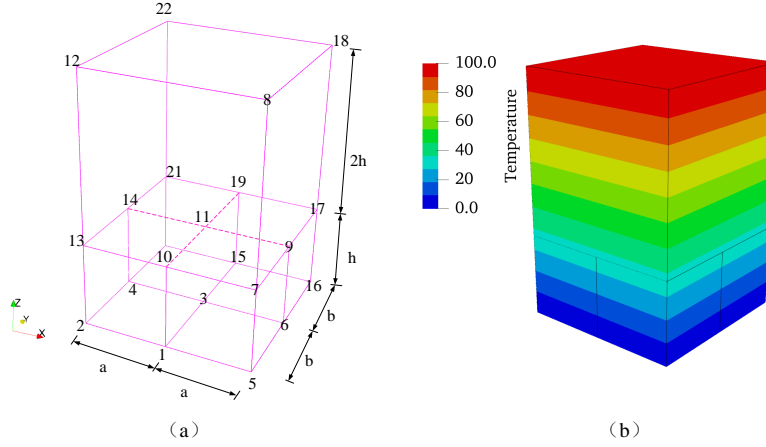


Fig. 10. Geometry model and temperature contour of the patch test (Unit: $^{\circ}\text{C}$).

Tab. 1. Maximum relative error of the nodal temperature.

Proposed method	Analytical solution	Relative error
33.3282	33.3333	1.53×10^{-4}

7.2. 3D heat conduction beam

In this example, we examined a 3D heat conduction problem, as illustrated in Fig. 11. The beam had a length of 6 m, with a width and height of 1.5 m. A temperature of $T = 70^{\circ}\text{C}$ was applied at the right boundary ($z = 0$ m), while a temperature of $T = 30^{\circ}\text{C}$ was imposed at the left boundary ($z = 6$ m). The material had a thermal conductivity of $1.0 \text{ W/m/}^{\circ}\text{C}$ and a volumetric heat capacity of $\rho c = 1.0 \text{ J}/(\text{m}^3 \cdot ^{\circ}\text{C})$.

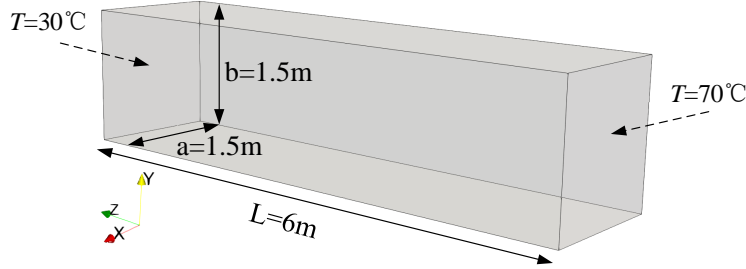


Fig. 11. Geometry and boundary conditions for a 3D heat conduction beam.

The domain was discretized using hexahedral, polyhedral and octree elements. A convergence study was conducted with all three types of mesh. We refined the meshes successively following the sequence $h = 1.0$ m, 0.5 m, 0.25 m, and 0.1 m, as shown in Fig. 12. Moreover, Fig. 12 (e) presented a cross-sectional view of a mesh layer along with several representative polyhedral elements. Fig. 13 showed that the PSBFEM and FEM exhibit a good convergence rate, with the accuracy of both methods increasing as the mesh was refined. When the mesh size was 0.1 m, the relative errors for the FEM, PSBFEM (polyhedral element) and PSBFEM (octree element) were 2.1×10^{-4} , 5.5×10^{-5} and 9.1×10^{-5} respectively. The relative errors of the PSBFEM were smaller than those of the FEM for the same element size. The relative errors for the polyhedral elements in PSBFEM were smaller than those for the octree elements at the same element size. This was mainly due to the fact that polyhedral elements have more nodes at the same element size. Moreover, Fig. 14 demonstrated a significant concurrence in the temperature

distribution between the PSBFEM and the analytical solution with refined meshes.

Additionally, Fig. 15 compared the computational cost of PSBFEM and FEM under the same degrees of freedom. To ensure a fair comparison, an automatic incrementation scheme was adopted to minimize the impact of increment size on solving time. The computation time was normalized for comparison. The computational cost of PSBFEM using the polyhedral element was slightly higher than that of the FEM, averaging approximately 1.70 times that of the FEM. This increase in computational cost can be attributed to the semi-analytical nature of SBFEM, which inherently involved more computations than FEM [31, 38]. In addition, by using acceleration technology, the computational time of PSBFEM with the octree mesh was smaller than that of FEM, averaging 0.53 times that of the FEM.

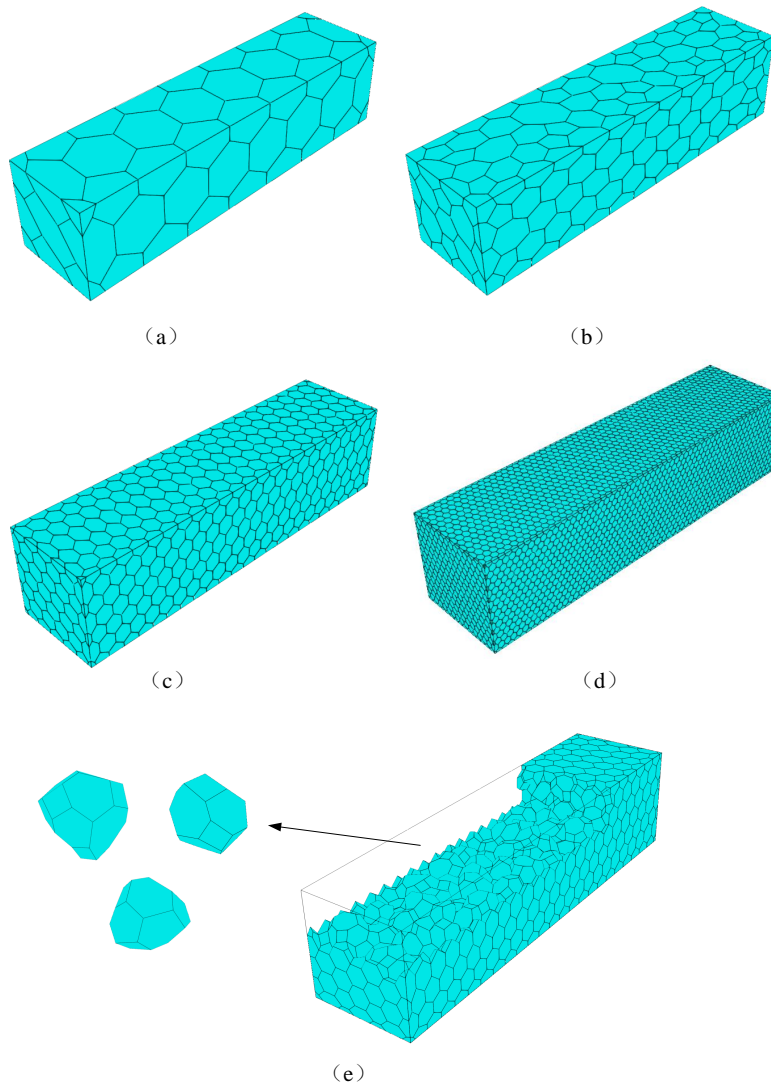


Fig. 12. Four levels of polyhedral mesh refinement: (a) 1.0 m mesh size; (b) 0.5 m mesh size; (c) 0.25 m mesh size; (d) 0.1 m mesh size; (e) internal element of the 0.25 m mesh size.

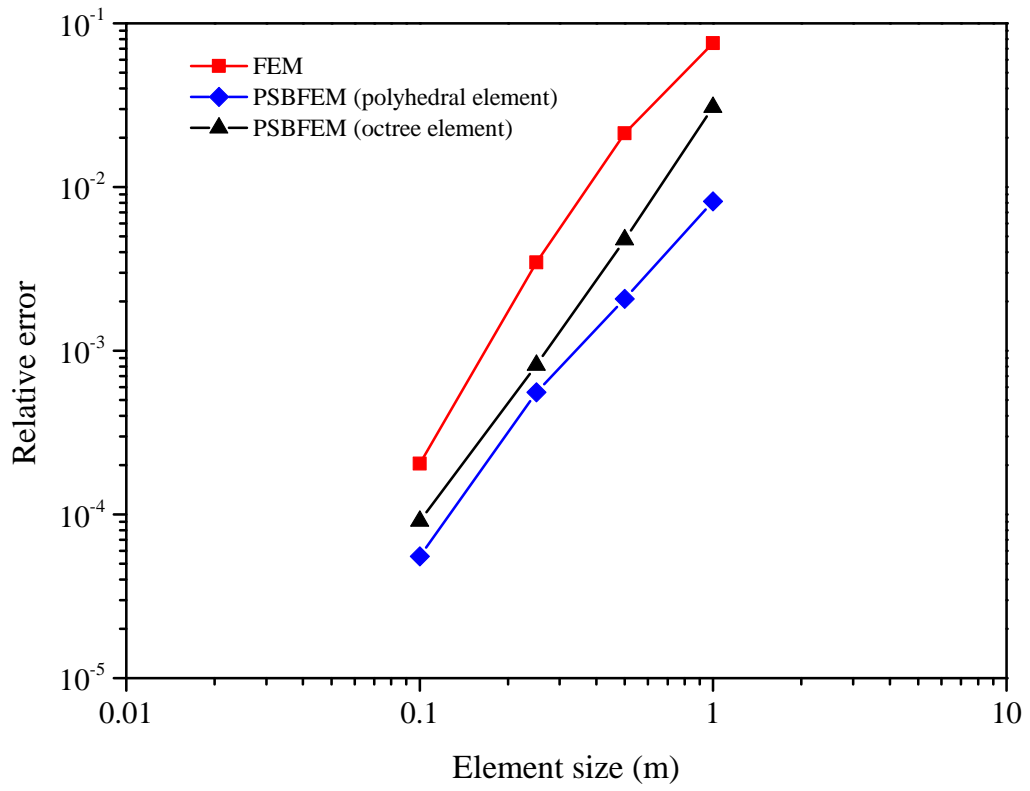


Fig. 13. Convergence of the relative errors in the temperature.

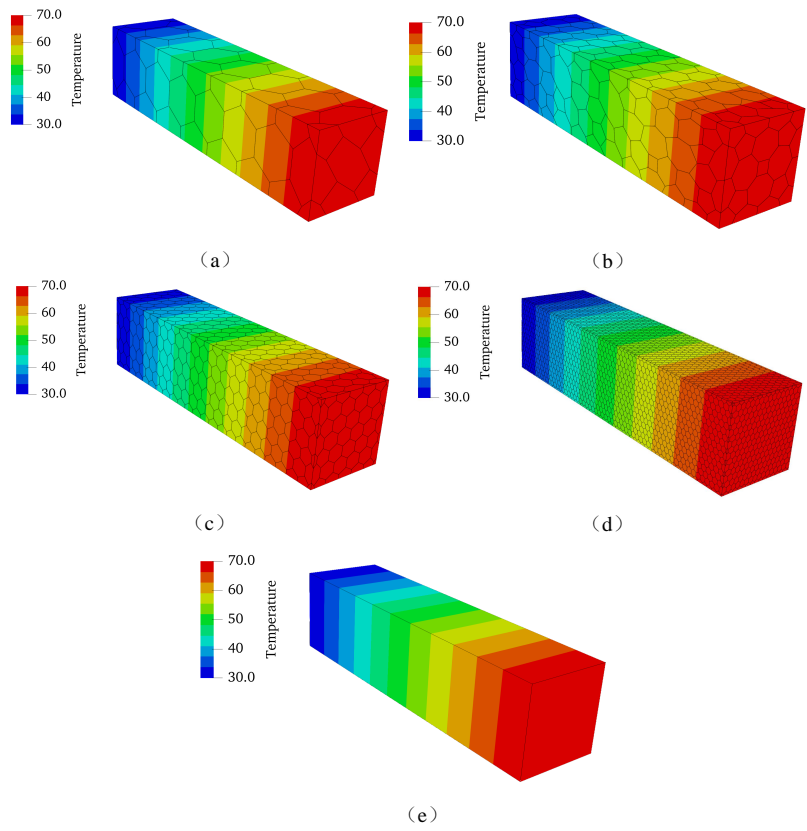


Fig. 14. Temperature distribution of the 3D heat conduction beam using polyhedral mesh refinement: (a) 1.0 m mesh size; (b) 0.5 m mesh size; (c) 0.25 m mesh size; (d) 0.1 m mesh size; (e) analytical solution (Unit: °C).

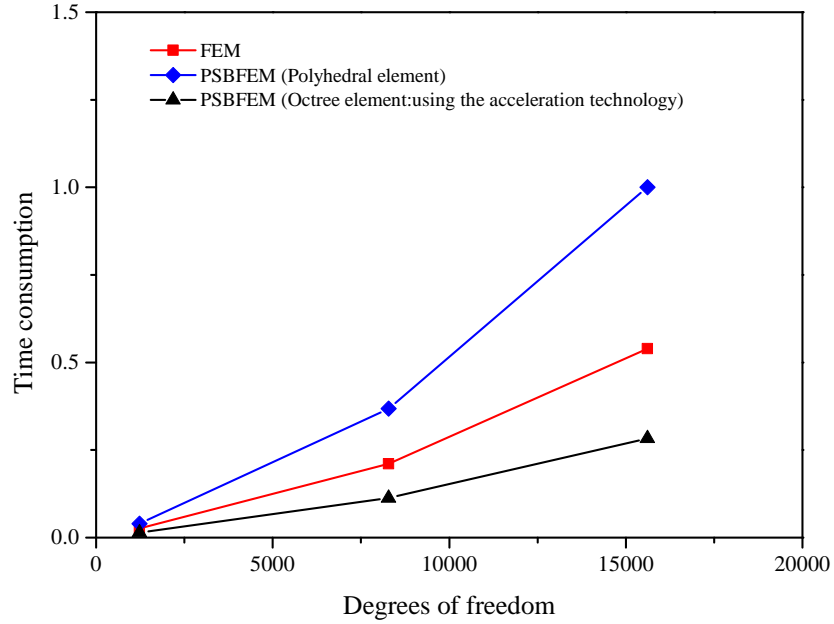


Fig. 15. Time consumption comparison for the steady-state heat conduction analysis.

To demonstrate the capability of octree mesh discretization in local mesh refinement, we discretized a 3D heat conduction beam using an octree mesh, as shown in Fig. 16. Figs. 16 (a) and 16 (b) represent the coarse and fine meshes, respectively, while Figs. 16 (c) and 16 (d) depict the local mesh refinement. In addition, Fig. 16 (e) presented a cross-section of local mesh refinement 2. Tab. 2 illustrated the mesh characteristics and relative errors for the local mesh refinement. The relative errors for local mesh refinement 2 and the fine mesh are both on the order of 10^{-4} , demonstrating a high level of computational accuracy. However, the computational time for local mesh refinement 2 was lower than that of the fine mesh. Thus, through local mesh refinement, refining the mesh in specific regions can yield more accurate

results while reducing computational time. As shown in Tab. 2, with the acceleration technology, the computational time of PBSFEM was significantly reduced, with an average reduction of 3 times in the computational time. Moreover, Fig. 17 also showed a close match in the temperature distribution between the analytical solution and the PSBFEM solution using the octree mesh for discretization.

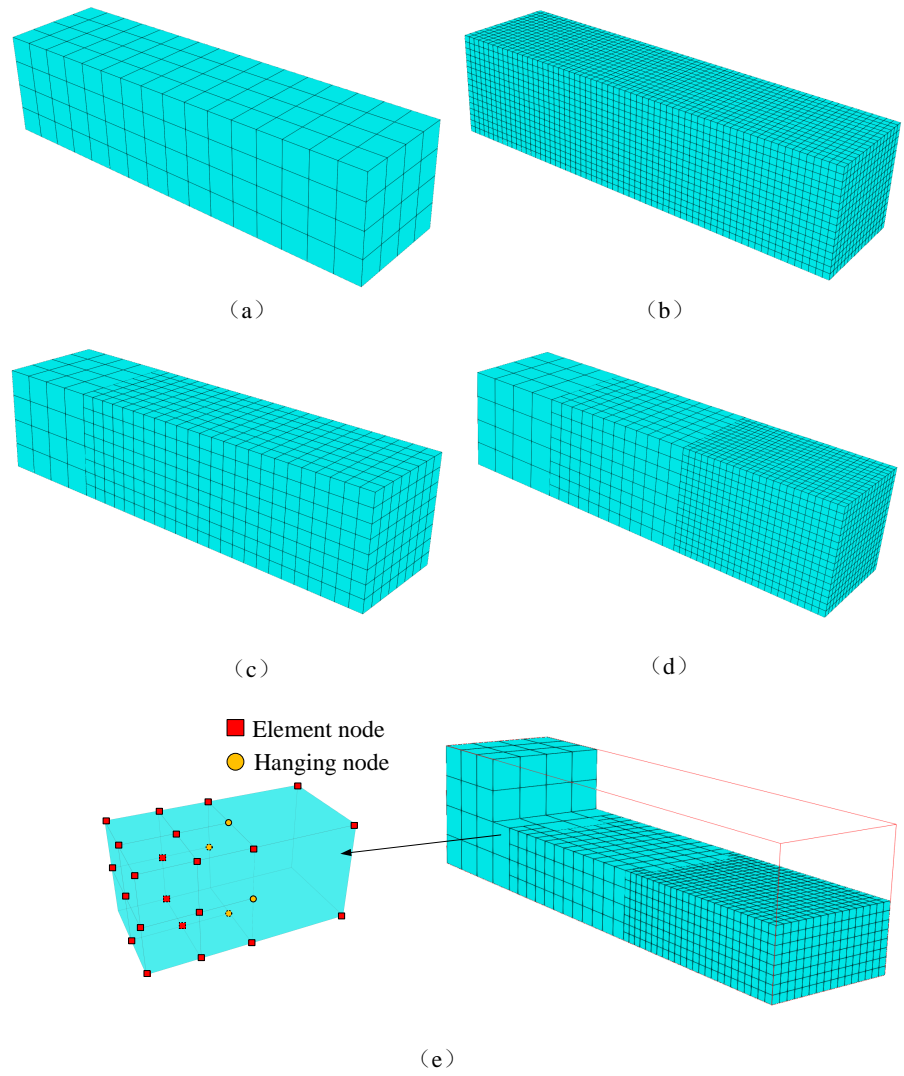


Fig. 16. Local mesh refinement model of the 3D heat conduction beam using the octree mesh: (a) coarse mesh; (b) fine mesh; (c) local mesh refinement 1; (d) local mesh refinement 2; (e) internal element of local mesh refinement 2.

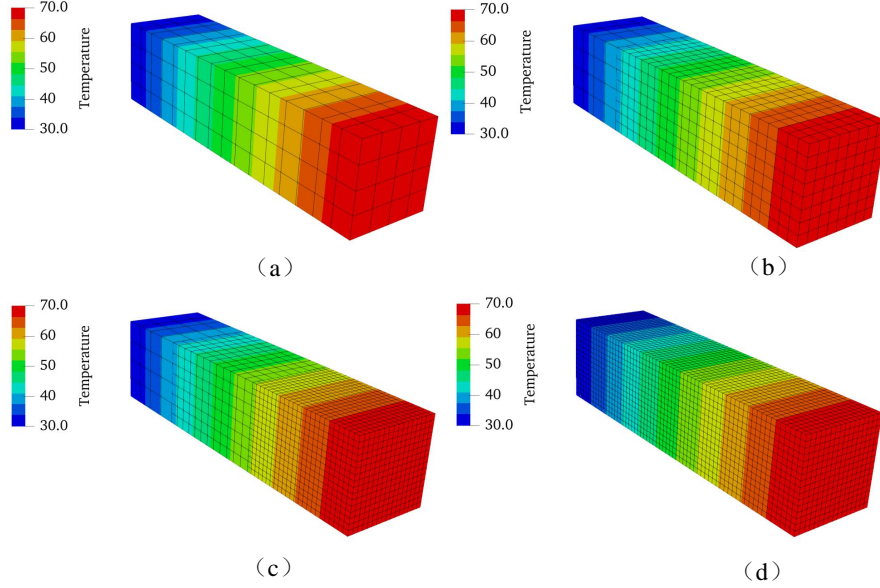


Fig. 17. Temperature distribution of the 3D conduction beam using the octree mesh: (a) temperature contour with coarse mesh; (b) temperature contour with local mesh refinement 1; (c) temperature contour with local mesh refinement 2; (d) temperature contour with fine mesh; (Unit: °C).

Tab. 2. Mesh characteristics, relative errors and time consumption.

Mesh type	Elements	Nodes	Faces	Relative error	CPU time (s)	CPU time (s)*
Coarse mesh	256	425	1536	1.78×10^{-2}	0.2	0.1
Fine mesh	8432	12141	53328	6.33×10^{-4}	9.2	3.1
Local mesh refinement 1	1572	2108	9504	2.80×10^{-3}	1.5	0.4
Local mesh refinement 2	6696	8063	40512	8.49×10^{-4}	6.2	1.8

Note: * denotes the use of acceleration technology based on the parent element.

7.3. Steady-state heat conduction

In this example, we considered a classical steady-state heat conduction problem, as shown in Fig. 18. The length, width, and height of the cube were all 1 m. The material had a thermal conductivity of 1.0 W/m/°C and

a volumetric heat capacity of $\rho c = 1.0 \text{ J}/(\text{m}^3 \cdot ^\circ \text{C})$. The boundary conditions of the cube were shown in Eq. (61).

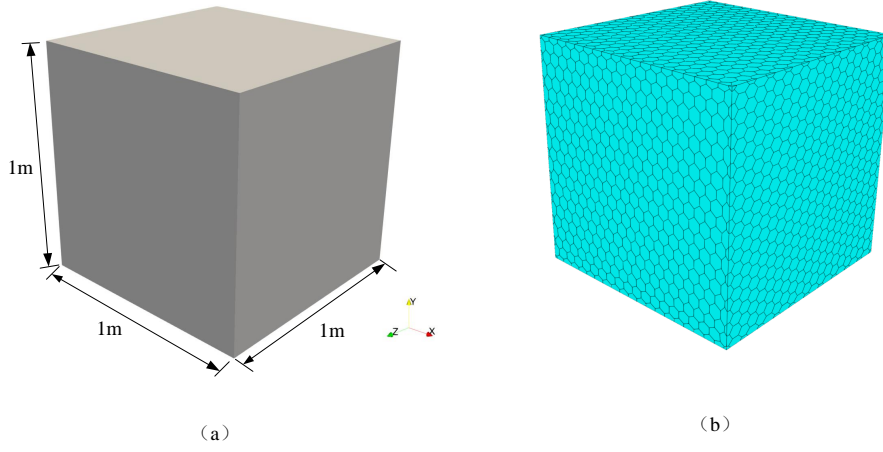


Fig. 18. A cube for the steady-state heat conduction problem: (a) the geometry model; (b) the mesh with a size of 0.05 m.

$$\begin{aligned}
 (x, y, z) \in \text{plane} \perp (x = 0), \quad T &= 0 \\
 (x, y, z) \in \text{plane} \perp (y = 0), \quad T &= 0 \\
 (x, y, z) \in \text{plane} \perp (z = 0), \quad T &= 0 \\
 (x, y, z) \in \text{plane} \perp (x = 1), \quad T &= 0 \\
 (x, y, z) \in \text{plane} \perp (y = 1), \quad T &= \sin(\pi x) \sin(\pi z) \\
 (x, y, z) \in \text{plane} \perp (z = 1), \quad T &= 0
 \end{aligned} \tag{61}$$

A convergence study was performed using mesh h -refinement, with successive refinements applied to mesh element sizes of 0.25 m, 0.1 m, 0.05 m, and 0.025 m. Fig. 18 (b) presented the polyhedral mesh with an element size

of 0.05 m. The analytical solution for the temperature at point P (x, y, z) within the domain was calculated based on the approach outlined in [61]:

$$T(x, y, z) = \frac{\sinh(\pi y)}{\sinh(\pi)} \sin(\pi x) \sin(\pi z). \quad (62)$$

The convergence of the relative error in temperature with mesh refinement was presented in Fig. 19. It is observed that the PSBFEM converges to the analytical solution at an optimal rate. Furthermore, the PSBFEM produces slightly more accurate results than the FEM for the same element size. Fig. 20 illustrated the temperature distribution for both FEM and PSBFEM, showing that the results of both methods closely match the analytical solution.

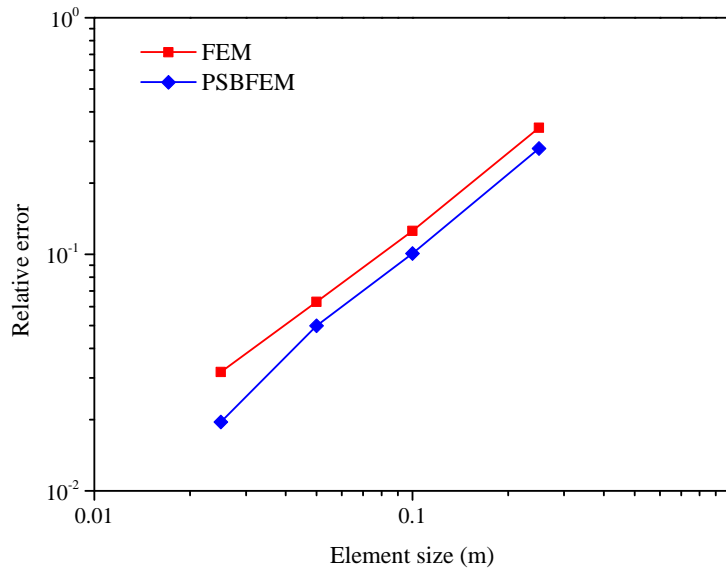


Fig. 19. Convergence of the relative error in temperature.

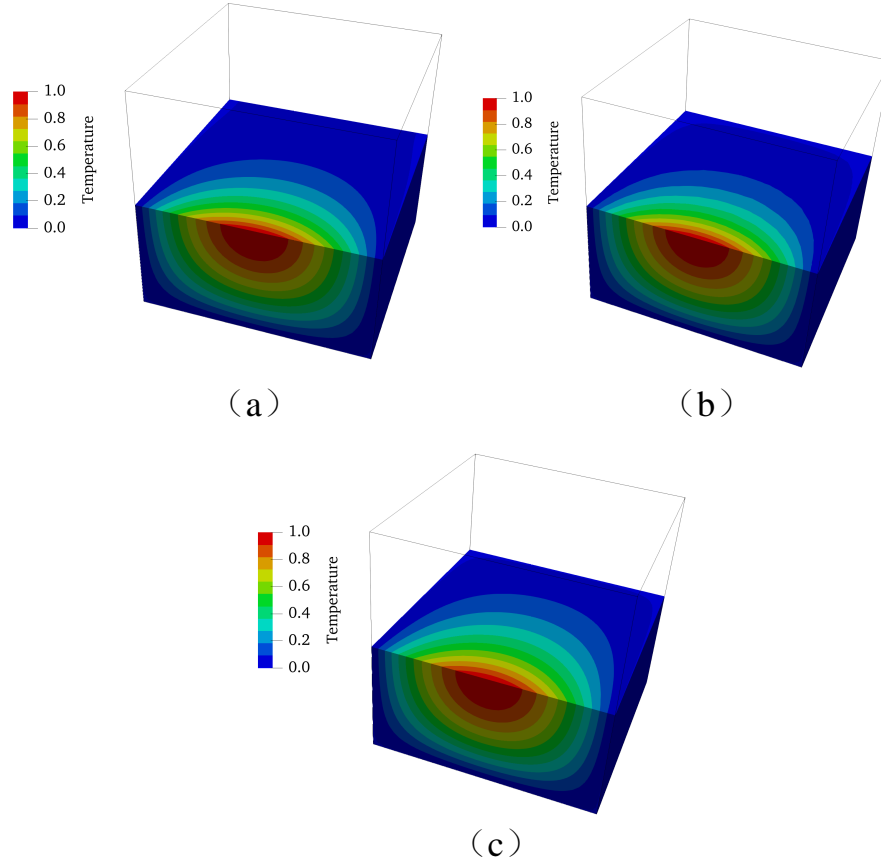


Fig. 20. Temperature distribution of a cube for the steady-state heat conduction problem: (a) FEM; (b) PSBFEM; (c) analytical solution; (Unit: °C).

7.4. Transient heat conduction

To validate the proposed PSBFEM for the transient heat conduction problem in three dimensions, we examined a cubic domain ($\pi \times \pi \times \pi$) with an analytical solution. The initial temperature distribution was defined as $T_0 = 10 \sin(x) \sin(y) \sin(z)$. Homogeneous Dirichlet boundary conditions were applied on all surfaces of the cube, assuming a constant temperature of

zero. The thermal properties of the material were given by a thermal conductivity $k = 1.0 \text{ W/m/}^\circ\text{C}$ and a volumetric heat capacity $\rho c = 1.0 \text{ J}/(\text{m}^3 \cdot ^\circ\text{C})$. The corresponding analytical solution for the temperature field was expressed as [62]:

$$T(x, y, z, t) = 10e^{-3t} \sin(x) \sin(y) \sin(z). \quad (63)$$

In both the PSBFEM and FEM simulations, a time step of $\Delta t = 0.01 \text{ s}$ was employed, with the total simulation time set to $t = 1 \text{ s}$. The computational domain was discretized using hexahedral, polyhedral and octree elements. To assess the accuracy and convergence of the method, a convergence study was conducted through progressive mesh refinement. The meshes were refined successively in the sequence of $\frac{\pi}{5}$, $\frac{\pi}{10}$, $\frac{\pi}{20}$, and $\frac{\pi}{40}$.

The comparison of the convergence rates was presented in Fig. 21. It is observed that the convergence rates of the PSBFEM and FEM were identical. At the same element size, the accuracy of the PSBFEM exceeded that of the FEM. The temperature-time history at the monitoring point ($x = \frac{\pi}{2}$, $y = \frac{\pi}{2}$, and $z = \frac{\pi}{2}$), obtained using the FEM and PSBFEM, was compared in Fig. 22, where both methods showed a good correspondence with the analytical solution. Furthermore, Fig. 23 illustrated the temperature distribution at different time steps for both the PSBFEM and FEM. The results of both methods were in excellent agreement with the analytical solution. Moreover, for transient problems, the computational time for both methods was shown in Fig. 24. Under the same degrees of freedom, the time required by PS-

BFEM using the polyhedral element was greater than that of FEM, averaging 1.87 times that of FEM. Additionally, with the application of acceleration technology, the computational time for PSBFEM using the octree mesh was reduced to, on average, 58% of the time required by FEM.

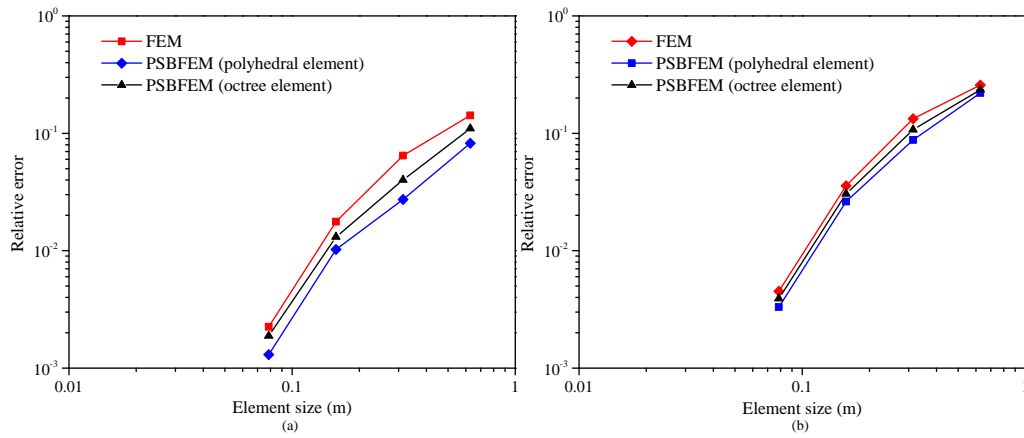


Fig. 21. Convergence of the relative error in temperature at different times: (a) $t = 0.5$ s; (b) $t = 1.0$ s.

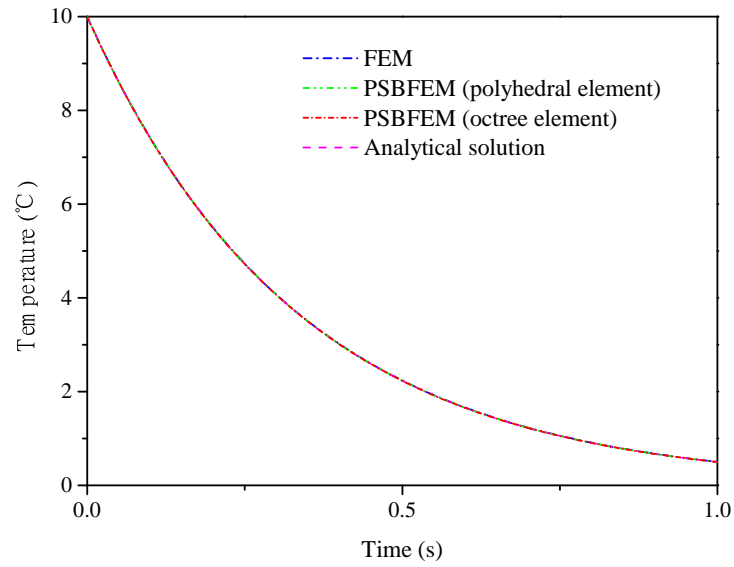


Fig. 22. Comparison of the temperature time history at the monitoring point.

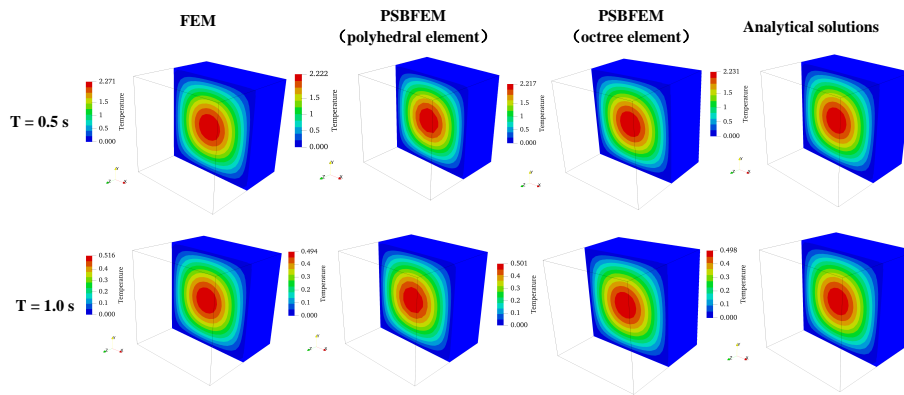


Fig. 23. Distribution of the temperature at different times; (Units:°C).

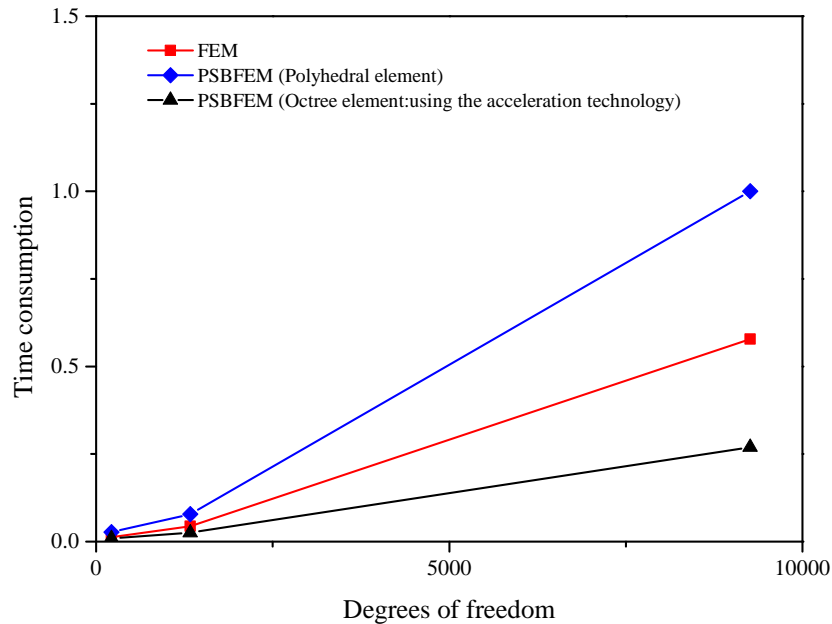


Fig. 24. Time consumption comparison for the transient heat conduction analysis.

7.5. Complex geometry analysis

With the rapid advancement of 3D printing, rapid prototyping, and digital analysis, the adoption of the STL format in finite element mesh generation had become increasingly essential. The simplicity and compatibility of the STL format allow efficient representation of complex 3D geometries. In this study, polyhedral meshes and octree-based meshes were utilized to automatically partition STL models, demonstrating the capability of PSBFEM to handle arbitrarily complex polyhedral elements.

7.5.1. Stanford's bunny using the polyhedral mesh

In this example, a Stanford bunny [63] given in STL format was used with a polyhedral mesh [64], as shown in Fig. 25 (b). To further highlight

the advantages of the polyhedral mesh, the model was also discretized using an unstructured tetrahedral mesh, as shown in Fig. 25 (c). The material properties were as follows: thermal conductivity of $52 \text{ W/m/}^\circ\text{C}$, specific heat of $434 \text{ J/kg/}^\circ\text{C}$, and density of 7800 kg/m^3 . A temperature of $T = 1000^\circ\text{C}$ was prescribed on the bottom of the model, while an initial temperature of $T_0 = 20^\circ\text{C}$ was applied throughout the entire model.

Tab. 3 presented a comparison between polyhedral and tetrahedral meshes based on several key metrics, including the number of nodes, elements, and surfaces. When using the same element size, the polyhedral mesh consists of 40,714 nodes, whereas the tetrahedral mesh contains only 7,132 nodes. Hence, the polyhedral mesh had a greater number of nodes at the same element size. Additionally, the polyhedral mesh requires only 132.60 seconds of CPU time, compared to the significantly higher 565.20 seconds required by the tetrahedral mesh. This suggested that polyhedral meshes could be a more effective choice for complex simulations, offering reduced computational costs. Furthermore, Fig. 26 illustrated that the temperature distributions for Stanford's bunny using the two different element types exhibited remarkable agreement.

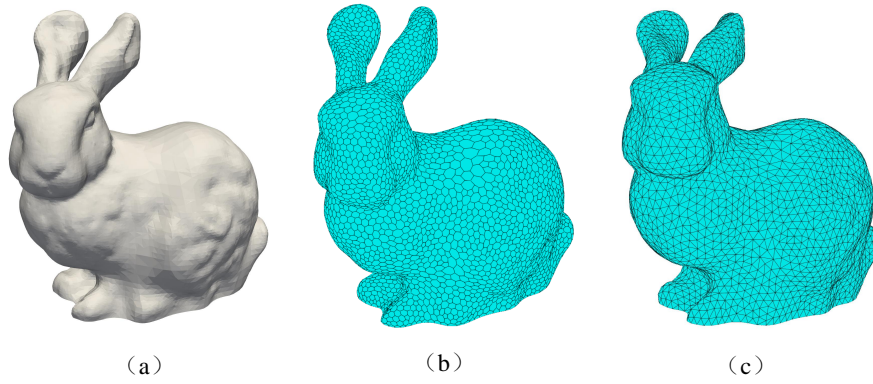


Fig. 25. Geometry and mesh model of Stanford's bunny; (a) the geometry model; (b) the polyhedral mesh; (c) the tetrahedral mesh.

Tab. 3. Mesh characteristics and relative errors of polyhedral and tetrahedral meshes.

Element type	Nodes	Elements	Surfaces	CPU time (s)
Polyhedron mesh	40714	7202	91879	132.60
Tetrahedral mesh	7132	32923	131692	565.20

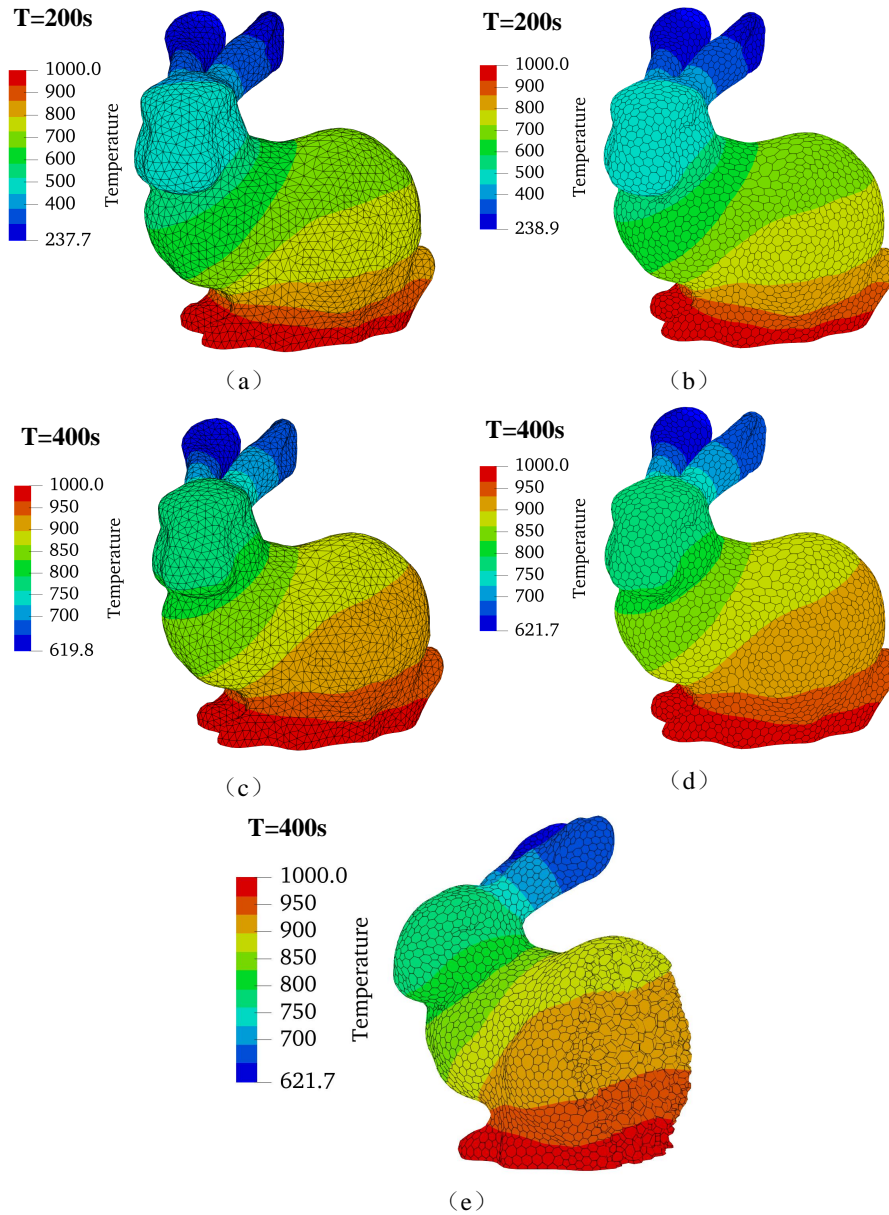


Fig. 26. Temperature distribution of Stanford's bunny using the PSBFEM: (a) temperature contour with tetrahedral elements at 200 s; (b) temperature contour with polyhedral elements at 200 s; (c) temperature contour with tetrahedral elements at 400 s; (d) temperature contour with polyhedral elements at 400 s; (e) localized contour of selected polyhedral elements from (d) at 400 s; (Units:°C).

7.5.2. Stanford's luck using the hybrid octree mesh

The hybrid octree mesh was a mesh generation method that combines hexahedral (cubic) elements with other types of elements, such as tetrahedra and polyhedra. For more detailed information, please refer to the relevant literature [65]. In this example, Stanford's luck [63] was used with the hybrid octree mesh algorithm, as shown in Fig. 27 (b). The cross-section of the hybrid octree mesh was illustrated in Fig. 28, which showed that the interior of the model was partitioned using a cubic octree mesh, while the outer boundary was formed by generating hybrid elements through a cutting process.

The material properties were defined as: a thermal conductivity of 60 W/m/°C, a specific heat of 97 J/kg/°C, and a density of 2000 kg/m³. A temperature of $T = 50^{\circ}\text{C}$ was applied to the bottom of Stanford's luck, while a temperature of $T = 100^{\circ}\text{C}$ was set on the torch of the model. Tab. 4 presented the composition of the hybrid octree mesh. The mesh was made up of 68.7% octree elements and 31.3% hybrid elements. Since the majority of the mesh consisted of high-quality cubic elements, the hybrid octree mesh achieved a high level of accuracy.

Moreover, Tab. 5 provided a comparison between the hybrid octree mesh and the tetrahedral mesh. The hybrid octree mesh contained more nodes but fewer elements and surfaces compared to the tetrahedral mesh. The computational cost of the hybrid octree mesh was significantly lower than that of the tetrahedral mesh. [Additionally, through acceleration technology, the](#)

computational time was significantly reduced. Fig. 29 showed the temperature distribution for Stanford's bunny using both mesh types, demonstrating a high degree of agreement between the results.

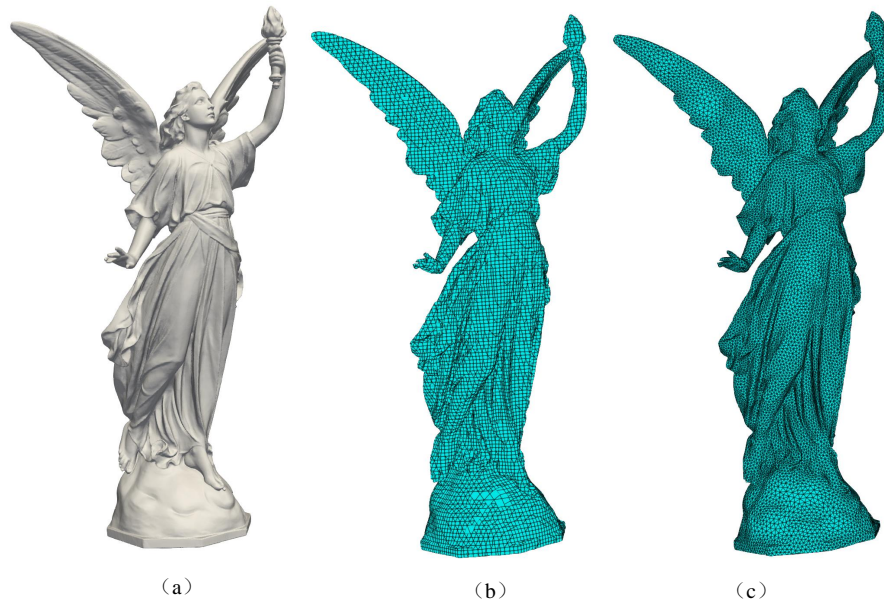


Fig. 27. Geometry and mesh model of Stanford's luck: (a) the geometry model; (b) the hybrid octree mesh; (c) the tetrahedral mesh.

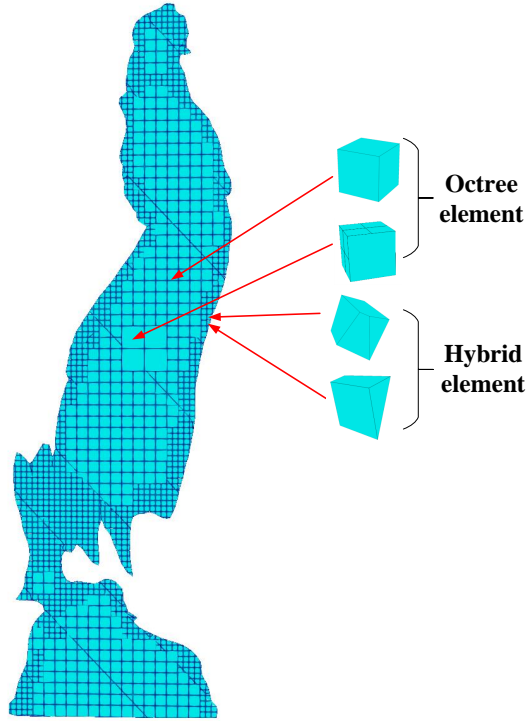


Fig. 28. Cross-section view of the hybrid octree mesh for Stanford's luck.

Tab. 4. Composition of hybrid octree mesh for the Stanford's luck.

Element type	octree element	hybrid element
Number of elements	32939	15020
Proportion	68.7%	31.3%

Tab. 5. Mesh characteristics, relative errors and time consumption.

Element type	Nodes	Elements	Surfaces	CPU time (s)	CPU time (s)*
Hybrid octree mesh	60579	47959	293594	209.6	98.7
Tetrahedral mesh	48684	222210	888840	859.4	—

Note: * denotes the use of acceleration technology based on the parent element.

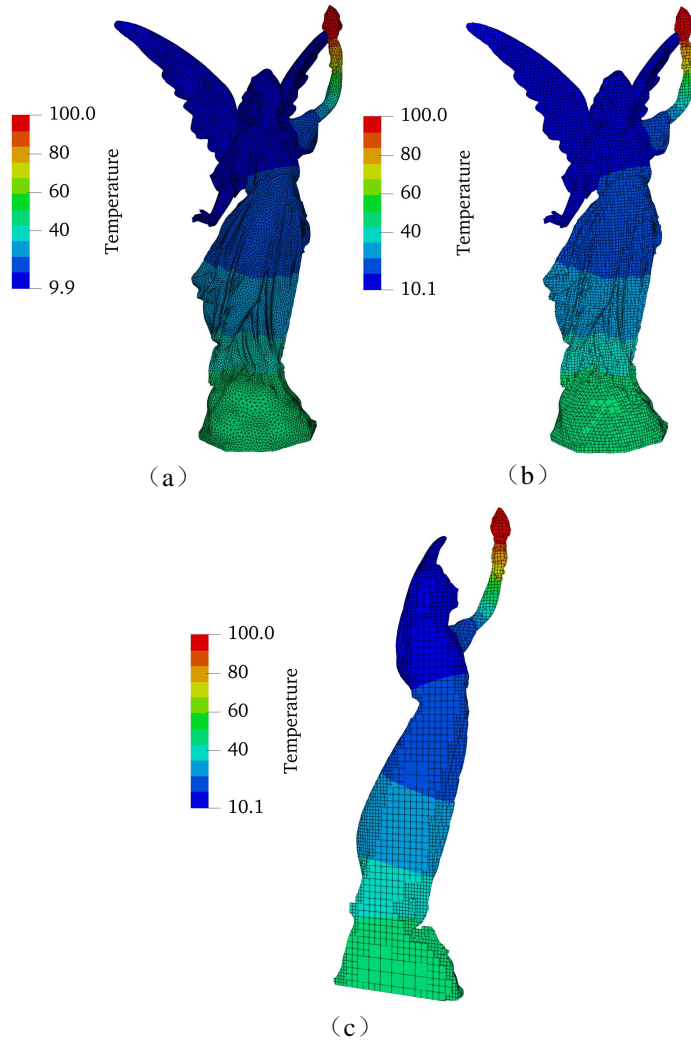


Fig. 29. Temperature distribution of Stanford's luck. (a) temperature contour with tetrahedral elements; (b) temperature contour with hybrid octree elements; (c) localized contour of selected hybrid octree element; (Units:°C).

8. Conclusions

This paper presented a PSBFEM framework that demonstrated considerable advantages in solving three-dimensional steady-state and transient heat

conduction problems. The key findings of this work are summarized as follows:

(1) By introducing polyhedral elements and utilizing Wachspress shape functions, the proposed method improved mesh efficiency, allowing for accurate solutions with fewer computational elements. This approach reduced preprocessing time, especially for complex geometries where traditional FEM methods would have required extensive re-meshing.

(2) Numerical results demonstrated that the PSBFEM could achieve high accuracy, even with coarse meshes. In particular, the method outperformed traditional FEM in terms of convergence rates, with lower relative errors observed in both steady-state and transient heat conduction problems.

(3) The method's ability to handle complex geometrical models, such as the Stanford Bunny, further highlighted its versatility. Compared to hexahedral mesh, polyhedral meshes not only provided better accuracy but also significantly reduced computational times, showcasing the potential of this method for large-scale industrial applications.

(4) The hybrid octree mesh structure, in combination with SBFEM, enabled efficient local refinement analysis. This approach offered a balance between accuracy and computational cost, making it suitable for applications requiring high-resolution analysis in localized regions while maintaining global solution stability. [Moreover, by utilizing the octree mesh parent element acceleration technique, the computational efficiency of PSBFEM was significantly enhanced, resulting in a reduction of computation time by 0.53](#)

to 0.58 times compared to the FEM.

In this study, we only considered the use of octree elements without hanging nodes to accelerate the computation. To fully leverage the performance of the octree mesh, future research will consider incorporating octree meshes with hanging nodes as a basic element type. Moreover, future work could explore extending this framework to other types of physical problems, including thermal stress and multiphysics scenarios. Moreover, implementing adaptive meshing strategies within the PSBFEM framework could further enhance its applicability to real-time engineering simulations.

9. Acknowledgements

The National Natural Science Foundation of China (grant NO. 42167046), the Yunnan Province Xing Dian Talent Support Program (grant NO. XDYC-QNRC-2022-0764) and Yunan Fundamental Research Projects (grant NO. 202401CF070043) provided support for this study.

Appendix A. The scaled boundary finite element equation for heat conduction problems

The weighted residual method is employed by multiplying Eq. (8) with the weighting function $w = w(\xi, \eta, \zeta)$ and integrating over the entire domain. A domain Ω is considered, where an element on the boundary is scaled within the range $\xi_1 \leq \xi \leq \xi_2$. Eq. (8) can be separated into three terms W_I , W_{II} ,

and W_{III} [27, 44]

$$\begin{aligned}
& \underbrace{\int_{\Omega} w \mathbf{b}_1^T \tilde{\mathbf{q}}_{,\xi} \, d\Omega}_{W_I} + \underbrace{\int_{\Omega} w \frac{1}{\xi} (\mathbf{b}_2^T \tilde{\mathbf{q}}_{,\eta} + \mathbf{b}_3^T \tilde{\mathbf{q}}_{,\zeta}) \, d\Omega}_{W_{II}} \\
& + i\omega \underbrace{\int_{\Omega} w \rho c \tilde{T} \, d\Omega}_{W_{III}} = 0.
\end{aligned} \tag{A.1}$$

The infinitesimal volume $d\Omega$ can be expressed as

$$d\Omega = \xi^2 |\mathbf{J}| d\xi d\eta d\zeta. \tag{A.2}$$

Substituting Eq. (A.2) into the first and third terms of Eq. (A.1), we obtain the following expressions. The first term, W_I , is given by

$$W_I = \int_{\xi_1}^{\xi_2} \xi^2 \int_{S_\xi} w \mathbf{b}_1^T \tilde{\mathbf{q}}_{,\xi} |\mathbf{J}| d\eta d\zeta d\xi. \tag{A.3}$$

Similarly, the third term can be written as

$$W_{III} = \int_{\xi_1}^{\xi_2} i\omega \xi^2 \int_{S_\xi} w \rho c \tilde{T} |\mathbf{J}| d\eta d\zeta d\xi. \tag{A.4}$$

For the second term W_{II} , applying Green's theorem to the surface integral

over S^ξ converts the integral into a contour integral, resulting in [27]

$$W_{II} = \int_{\xi_1}^{\xi_2} \xi \left(\oint_{\Gamma^\xi} w (q_n^\zeta g^\zeta d\eta + q_n^\eta g^\eta d\zeta) - \int_{S^\xi} (-2w \mathbf{b}_1^T + w_{,\eta} \mathbf{b}_2^T + w_{,\zeta} \mathbf{b}_3^T) \tilde{\mathbf{q}} |\mathbf{J}| d\eta d\zeta \right) d\xi, \quad (\text{A.5})$$

where q_n^ζ and q_n^η are the amplitude of the normal flux on the surfaces. g^ζ and g^η are the magnitude of outward normal vectors to the surfaces.

Substituting Eqs. (A.3), (A.5), and (A.4) into Eq. (A.1), we obtain

$$\begin{aligned} & \int_{\xi_1}^{\xi_2} \left(\xi^2 \int_{S_\xi} w \mathbf{b}_1^T \tilde{\mathbf{q}}_{\mathbf{J},\xi} |\mathbf{J}| d\eta d\zeta + \xi \oint_{\Gamma^\xi} w (q_n^\zeta g^\zeta d\eta + q_n^\eta g^\eta d\zeta) \right. \\ & \quad \left. - \xi \int_{S^\xi} (-2w \mathbf{b}_1^T + w_{,\eta} \mathbf{b}_2^T + w_{,\zeta} \mathbf{b}_3^T) \tilde{\mathbf{q}} |\mathbf{J}| d\eta d\zeta \right. \\ & \quad \left. + i\omega \xi^2 \int_{S_\xi} w \rho c \tilde{T} |\mathbf{J}| d\eta d\zeta \right) d\xi = 0. \end{aligned} \quad (\text{A.6})$$

Eq. (A.6) holds when the integrand of the integral over ξ equal to zero [27]

$$\begin{aligned} & \xi^2 \int_{S_\xi} w \mathbf{b}_1^T \tilde{\mathbf{q}}_{\mathbf{J},\xi} |\mathbf{J}| d\eta d\zeta + \xi \oint_{\Gamma^\xi} w (q_n^\zeta g^\zeta d\eta + q_n^\eta g^\eta d\zeta) \\ & \quad - \xi \int_{S^\xi} (-2w \mathbf{b}_1^T + w_{,\eta} \mathbf{b}_2^T + w_{,\zeta} \mathbf{b}_3^T) \tilde{\mathbf{q}} |\mathbf{J}| d\eta d\zeta \\ & \quad + i\omega \xi^2 \int_{S_\xi} w \rho c \tilde{T} |\mathbf{J}| d\eta d\zeta = 0. \end{aligned} \quad (\text{A.7})$$

The weighting function $w = w(\xi, \eta, \zeta)$ is constructed in the same way as

the temperature field in Eq. (21)

$$w(\xi, \eta, \zeta) = \mathbf{N}(\eta, \zeta)w(\xi). \quad (\text{A.8})$$

By substituting Eq. (A.8) into Eq. (A.7) for an arbitrary $w(\xi)$, we obtain

$$\begin{aligned} & \xi^2 \int_{S^\xi} \mathbf{B}_1^T \tilde{\mathbf{q}}_{,\xi} |\mathbf{J}| d\eta d\zeta - \xi \int_{S^\xi} (-2\mathbf{B}_1^T + \mathbf{B}_2^T) \tilde{\mathbf{q}} |\mathbf{J}| d\eta d\zeta \\ & + i\omega \xi^2 \int_{S^\xi} \mathbf{N}(\eta, \zeta)^T \rho c |\mathbf{J}| d\eta d\zeta \\ & - \xi \oint_{\Gamma^\xi} \mathbf{N}(\eta, \zeta)^T (q_n^\zeta g^\zeta d\eta + q_n^\eta g^\eta d\zeta) = 0. \end{aligned} \quad (\text{A.9})$$

Substituting the Eq. (26) into Eq. (A.9), we obtain

$$\begin{aligned} & \xi^2 \int_{S^\xi} \mathbf{B}_1^T \mathbf{k} \left(\mathbf{B}_1 \tilde{T}_{,\xi\xi} + \frac{1}{\xi} \mathbf{B}_2 \tilde{T}_{,\xi} - \frac{1}{\xi^2} \mathbf{B}_2 \tilde{T} \right) |\mathbf{J}| d\eta d\zeta - \\ & \xi \int_{S^\xi} (-2\mathbf{B}_1^T + \mathbf{B}_2^T) \mathbf{k} \left(\mathbf{B}_1 \tilde{T}_{,\xi} + \frac{1}{\xi} \mathbf{B}_2 \tilde{T} \right) |\mathbf{J}| d\eta d\zeta - \\ & i\omega \xi^2 \int_{S^\xi} \mathbf{N}(\eta, \zeta)^T \rho c \mathbf{N}(\eta, \zeta) \tilde{T} |\mathbf{J}| d\eta d\zeta - \xi \mathbf{F}(\xi) = 0. \end{aligned} \quad (\text{A.10})$$

Introducing the coefficient matrices

$$\mathbf{E}_0 = \int_{S_e} \mathbf{B}_1^T \mathbf{k} \mathbf{B}_1 |\mathbf{J}| d\eta d\zeta, \quad (\text{A.11})$$

$$\mathbf{E}_1 = \int_{S_e} \mathbf{B}_2^T \mathbf{k} \mathbf{B}_1 |\mathbf{J}| d\eta d\zeta, \quad (\text{A.12})$$

$$\mathbf{E}_2 = \int_{S_e} \mathbf{B}_2^T \mathbf{k} \mathbf{B}_2 |\mathbf{J}| d\eta d\zeta, \quad (\text{A.13})$$

$$\mathbf{M}_0 = \int_{S_e} \mathbf{N}^T \rho c \mathbf{N} |\mathbf{J}| d\eta d\zeta, \quad (\text{A.14})$$

and

$$\mathbf{F}(\xi) = \int_{\xi_1}^{\xi_2} [\mathbf{N}(\eta(\xi), \zeta(\xi))]^T \left(q_n^\xi g^\xi \frac{d\eta}{d\xi} + q_n^\eta g^\eta \frac{d\zeta}{d\xi} \right) d\xi, \quad (\text{A.15})$$

yields

$$\begin{aligned} & \mathbf{E}_0 \xi^2 \tilde{T}(\xi)_{,\xi\xi} + (2\mathbf{E}_0 - \mathbf{E}_1 + \mathbf{E}_1^T) \xi \tilde{T}(\xi)_{,\xi} \\ & + (\mathbf{E}_1^T - \mathbf{E}_2) \tilde{T}(\xi) - \mathbf{M}_0 i \omega \xi^2 \tilde{T}(\xi) - \xi \mathbf{F}(\xi) = 0. \end{aligned}$$

References

- [1] Z. Zhang, X. Wang, Y. Yan, A review of the state-of-the-art in electronic cooling, *e-Prime-Advances in Electrical Engineering, Electronics and Energy* 1 (2021) 100009.
- [2] S. P. Murzin, N. L. Kazanskiy, C. Stiglbrunner, Analysis of the Advantages of Laser Processing of Aerospace Materials Using Diffractive Optics, *Metals* 11 (6) (2021) 963. doi:10.3390/met11060963.
- [3] Z. Tian, X. Liu, C. Wang, D. Zhang, W. Tian, S. Qiu, G. Su, Experimental investigation on the heat transfer performance of high-temperature potassium heat pipe for nuclear reactor, *Nuclear Engineering and Design* 378 (2021) 111182.
- [4] L. D. Hung Anh, Z. Pásztor, An overview of factors influencing ther-

- mal conductivity of building insulation materials, *Journal of Building Engineering* 44 (2021) 102604. doi:10.1016/j.jobbe.2021.102604.
- [5] C. Shi, Y. Wang, C. Xu, Experimental study and analysis on heat transfer coefficient of radial heat pipe, *Journal of Thermal Science* 19 (5) (2010) 425–429. doi:10.1007/s11630-010-0404-y.
- [6] S. Yang, J. Wang, G. Dai, F. Yang, J. Huang, Controlling macroscopic heat transfer with thermal metamaterials: Theory, experiment and application, *Physics Reports* 908 (2021) 1–65. doi:10.1016/j.physrep.2020.12.006.
- [7] W. Pophillat, G. Attard, P. Bayer, J. Hecht-Méndez, P. Blum, Analytical solutions for predicting thermal plumes of groundwater heat pump systems, *Renewable Energy* 147 (2020) 2696–2707. doi:10.1016/j.renene.2018.07.148.
- [8] A. Hobiny, I. Abbas, Analytical solutions of fractional bioheat model in a spherical tissue, *Mechanics Based Design of Structures and Machines* 49 (3) (2021) 430–439. doi:10.1080/15397734.2019.1702055.
- [9] M. Malek, N. Izem, M. Seaid, et al., A three-dimensional enriched finite element method for nonlinear transient heat transfer in functionally graded materials, *International Journal of Heat and Mass Transfer* 155 (2020) 119804.

- [10] S. Bilal, R. Mahmood, A. Majeed, I. Khan, K. S. Nisar, Finite element method visualization about heat transfer analysis of newtonian material in triangular cavity with square cylinder, *Journal of Materials Research and Technology* 9 (3) (2020) 4904–4918.
- [11] J. A. Cottrell, T. J. Hughes, Y. Bazilevs, *Isogeometric analysis: toward integration of CAD and FEA*, John Wiley & Sons, 2009.
- [12] E. Majchrzak, B. Mochnacki, The bem application for numerical solution of non-steady and nonlinear thermal diffusion problems, *Computer Assisted Methods in Engineering and Science* 3 (4) (2023) 327–346.
- [13] T. Yu, B. Chen, S. Natarajan, T. Q. Bui, A locally refined adaptive isogeometric analysis for steady-state heat conduction problems, *Engineering Analysis with Boundary Elements* 117 (2020) 119–131.
- [14] M. Afrasiabi, M. Roethlin, K. Wegener, Contemporary meshfree methods for three dimensional heat conduction problems, *Archives of Computational Methods in Engineering* 27 (2020) 1413–1447.
- [15] S. Cai, Z. Wang, S. Wang, P. Perdikaris, G. E. Karniadakis, Physics-informed neural networks for heat transfer problems, *Journal of Heat Transfer* 143 (6) (2021) 060801.
- [16] S. Li, X. Cui, N-sided polygonal smoothed finite element method (nsfem) with non-matching meshes and their applications for brittle fracture

- problems, *Computer Methods in Applied Mechanics and Engineering* 359 (2020) 112672.
- [17] M. Lacroix, S. Février, E. Fernández, L. Papeleux, R. Boman, J.-P. Ponthot, A comparative study of interpolation algorithms on non-matching meshes for pfem-fem fluid-structure interactions, *Computers & Mathematics with Applications* 155 (2024) 51–65.
- [18] B. V. Damirchi, M. R. Carvalho, L. A. Bitencourt Jr, O. L. Manzoli, D. Dias-da Costa, Transverse and longitudinal fluid flow modelling in fractured porous media with non-matching meshes, *International Journal for Numerical and Analytical Methods in Geomechanics* 45 (1) (2021) 83–107.
- [19] E. Ooi, H. Man, S. Natarajan, C. Song, Adaptation of quadtree meshes in the scaled boundary finite element method for crack propagation modelling, *Engineering Fracture Mechanics* 144 (2015) 101–117.
- [20] W. Sun, Z. Cai, J. Choo, Mixed arlequin method for multiscale poromechanics problems, *International Journal for Numerical Methods in Engineering* 111 (7) (2017) 624–659.
- [21] M. Zhou, B. Zhang, T. Chen, C. Peng, H. Fang, A three-field dual mortar method for elastic problems with nonconforming mesh, *Computer Methods in Applied Mechanics and Engineering* 362 (2020) 112870.

- [22] L. Jendele, J. Červenka, On the solution of multi-point constraints–application to fe analysis of reinforced concrete structures, *Computers & Structures* 87 (15-16) (2009) 970–980.
- [23] S. Biabanaki, A. Khoei, A polygonal finite element method for modeling arbitrary interfaces in large deformation problems, *Computational Mechanics* 50 (2012) 19–33.
- [24] H. Chi, C. Talischi, O. Lopez-Pamies, G. H. Paulino, Polygonal finite elements for finite elasticity, *International Journal for Numerical Methods in Engineering* 101 (4) (2015) 305–328.
- [25] H. Gravenkamp, A. A. Saputra, C. Song, C. Birk, Efficient wave propagation simulation on quadtree meshes using sbfem with reduced modal basis, *International Journal for Numerical Methods in Engineering* 110 (12) (2017) 1119–1141.
- [26] Y. Yang, Z. Zhang, Y. Feng, K. Wang, A novel solution for seepage problems implemented in the abaqus uel based on the polygonal scaled boundary finite element method, *Geofluids* 2022 (1) (2022) 5797014.
- [27] C. Song, *The scaled boundary finite element method: introduction to theory and implementation*, John Wiley & Sons, 2018.
- [28] C. Song, E. T. Ooi, S. Natarajan, A review of the scaled boundary finite element method for two-dimensional linear elastic fracture mechanics, *Engineering Fracture Mechanics* 187 (2018) 45–73.

- [29] N. Ye, C. Su, Y. Yang, Free and forced vibration analysis in abaqus based on the polygonal scaled boundary finite element method, *Advances in Civil Engineering* 2021 (1) (2021) 7664870.
- [30] K. Chen, D. Zou, X. Kong, X. Yu, An efficient nonlinear octree sbfem and its application to complicated geotechnical structures, *Computers and Geotechnics* 96 (2018) 226–245.
- [31] N. Ye, C. Su, Y. Yang, PSBFEM-Abaqus: Development of User Element Subroutine (UEL) for Polygonal Scaled Boundary Finite Element Method in Abaqus, *Mathematical Problems in Engineering* 2021 (2021) 1–22. doi:10.1155/2021/6628837.
- [32] S. Natarajan, E. T. Ooi, A. Saputra, C. Song, A scaled boundary finite element formulation over arbitrary faceted star convex polyhedra, *Engineering Analysis with Boundary Elements* 80 (2017) 218–229.
- [33] X. Li, H. Su, Y. Wang, An improved polygon mesh generation and its application in sbfem using nurbs boundary, *Computational Mechanics* (2024) 1–19.
- [34] Q. Zang, S. P. Bordas, J. Liu, S. Natarajan, Nurbs-enhanced polygonal scaled boundary finite element method for heat diffusion in anisotropic media with internal heat sources, *Engineering Analysis with Boundary Elements* 148 (2023) 279–292. doi:https://doi.org/10.1016/j.enganabound.2022.12.028.

URL <https://www.sciencedirect.com/science/article/pii/S0955799722004829>

- [35] S. Ya, S. Eisenträger, C. Song, J. Li, An open-source ABAQUS implementation of the scaled boundary finite element method to study interfacial problems using polyhedral meshes, *Computer Methods in Applied Mechanics and Engineering* 381 (2021) 113766. doi:10.1016/j.cma.2021.113766.
- [36] Z. Yang, F. Yao, Y. Huang, Development of ABAQUS UEL/VUEL subroutines for scaled boundary finite element method for general static and dynamic stress analyses, *Engineering Analysis with Boundary Elements* 114 (2020) 58–73. doi:10.1016/j.enganabound.2020.02.004.
- [37] M. H. Baziyar, A. Talebi, Scaled boundary finite-element method for solving non-homogeneous anisotropic heat conduction problems, *Applied Mathematical Modelling* 39 (23-24) (2015) 7583–7599.
- [38] B. Yu, P. Hu, A. A. Saputra, Y. Gu, The scaled boundary finite element method based on the hybrid quadtree mesh for solving transient heat conduction problems, *Applied Mathematical Modelling* 89 (2021) 541–571.
- [39] Y. Yang, Z. Zhang, Y. Feng, Y. Yu, K. Wang, L. Liang, A polygonal scaled boundary finite element method for solving heat conduction problems, arXiv preprint arXiv:2106.12283 (2021).

- [40] Y. He, J. Guo, H. Yang, Image-based numerical prediction for effective thermal conductivity of heterogeneous materials: A quadtree based scaled boundary finite element method, *International Journal of Heat and Mass Transfer* 128 (2019) 335–343.
- [41] Y. He, X. Dong, H. Yang, A new adaptive algorithm for phase change heat transfer problems based on quadtree sbfem and smoothed effective heat capacity method, *Numerical Heat Transfer, Part B: Fundamentals* 75 (2) (2019) 111–126.
- [42] X. Wang, H. Yang, Y. He, A multiscale scaled boundary finite element method solving steady-state heat conduction problem with heterogeneous materials, *Numerical Heat Transfer, Part B: Fundamentals* 83 (6) (2023) 345–366.
- [43] S. Lu, J. Liu, G. Lin, P. Zhang, Modified scaled boundary finite element analysis of 3d steady-state heat conduction in anisotropic layered media, *International Journal of Heat and Mass Transfer* 108 (2017) 2462–2471.
- [44] C. Song, J. P. Wolf, The scaled boundary finite element method—alias consistent infinitesimal finite element cell method—for diffusion, *International Journal for Numerical Methods in Engineering* 45 (10) (1999) 1403–1431. doi:10.1002/(SICI)1097-0207(19990810)45:10<1403::AID-NME636>3.0.CO;2-E.
- [45] C. Song, A matrix function solution for the scaled boundary finite-

- element equation in statics, *Computer Methods in Applied Mechanics and Engineering* 193 (23-26) (2004) 2325–2356.
- [46] L. Perumal, A brief review on polygonal/polyhedral finite element methods, *Mathematical Problems in Engineering* 2018 (1) (2018) 5792372.
- [47] M. S. Floater, K. Hormann, G. Kós, A general construction of barycentric coordinates over convex polygons, *advances in computational mathematics* 24 (2006) 311–331.
- [48] N. Sukumar, E. A. Malsch, Recent advances in the construction of polygonal finite element interpolants, *Archives of Computational Methods in Engineering* 13 (2006) 129–163.
- [49] E. L. Wachspress, A rational basis for function approximation, in: *Conference on Applications of Numerical Analysis: Held in Dundee/Scotland, March 23–26, 1971*, Springer, 2006, pp. 223–252.
- [50] H. Nguyen-Xuan, S. Nguyen-Hoang, T. Rabczuk, K. Hackl, A polytree-based adaptive approach to limit analysis of cracked structures, *Computer Methods in Applied Mechanics and Engineering* 313 (2017) 1006–1039.
- [51] C.-T. Wu, S.-W. Wu, R.-P. Niu, C. Jiang, G. Liu, The polygonal finite element method for solving heat conduction problems, *Engineering Analysis with Boundary Elements* 155 (2023) 935–947.

- [52] J. Warren, On the uniqueness of barycentric coordinates, *Contemporary Mathematics* 334 (2003) 93–100.
- [53] J. Warren, S. Schaefer, A. N. Hirani, M. Desbrun, Barycentric coordinates for convex sets, *Advances in computational mathematics* 27 (2007) 319–338.
- [54] F. Li, P. Ren, A novel solution for heat conduction problems by extending scaled boundary finite element method, *International Journal of Heat and Mass Transfer* 95 (2016) 678–688. doi:<https://doi.org/10.1016/j.ijheatmasstransfer.2015.12.019>.
URL <https://www.sciencedirect.com/science/article/pii/S0017931015305640>
- [55] O. Zienkiewicz, R. Taylor, O. Zienkiewicz, R. Taylor, *The finite element method*, vol. 1 mcgraw-hill (1989).
- [56] ANSYS Inc., *ANSYS Fluent User’s Guide*, release 2023 R1, Canonsburg, PA, USA (2023).
- [57] Siemens Digital Industries Software, *STAR-CCM+ User Guide*, version 2023.1, Siemens PLM Software Inc., Plano, TX, USA (2023).
- [58] Kitware, Inc., *The ParaView Guide: A Parallel Visualization Application*, version 5.11, Clifton Park, NY, USA (2023).
- [59] D. Zou, K. Chen, X. Kong, X. Yu, An approach integrating bim, octree and fem-sbfem for highly efficient modeling and seismic damage analysis

- of building structures, *Engineering Analysis with Boundary Elements* 104 (2019) 332–346.
- [60] J. Zhang, S. Chauhan, Fast explicit dynamics finite element algorithm for transient heat transfer, *International Journal of Thermal Sciences* 139 (2019) 160–175. doi:10.1016/j.ijthermalsci.2019.01.030.
- [61] M. Afrasiabi, M. Roethlin, K. Wegener, Contemporary Meshfree Methods for Three Dimensional Heat Conduction Problems, *Archives of Computational Methods in Engineering* 27 (5) (2020) 1413–1447. doi:10.1007/s11831-019-09355-7.
- [62] G. Lin, P. Li, J. Liu, P. Zhang, Transient heat conduction analysis using the nurbs-enhanced scaled boundary finite element method and modified precise integration method, *Acta Mechanica Solida Sinica* 30 (2017) 445–464.
- [63] S. U. C. G. Laboratory, The stanford bunny, <https://graphics.stanford.edu/software/scanview/models/bunny.html>, accessed: 2024-10-06 (1994).
- [64] Y. Liu, A. A. Saputra, J. Wang, F. Tin-Loi, C. Song, Automatic polyhedral mesh generation and scaled boundary finite element analysis of STL models, *Computer Methods in Applied Mechanics and Engineering* 313 (2017) 106–132. doi:10.1016/j.cma.2016.09.038.

- [65] C. Song, The Scaled Boundary Finite Element Method: Introduction to Theory and Implementation, Wiley, Hoboken, NJ Chichester, West Sussex, 2018.